Two-Photon Vibrational Transitions in O_2^+

Addison D. Hartman

Advisor: Professor David A. Hanneke
May 13, 2022

Submitted to the
Department of Physics & Astronomy of Amherst College
in partial fulfilment of the
requirements for the degree of
Bachelors of Arts with honors

Abstract

The standard model of particle physics is unable to explain some prominent phenomena, including dark matter and gravity. Physicists in a variety of subfields are searching for physics beyond the standard model which is necessary for a complete picture of our universe. One approach to these types of questions is to use precision measurement of atomic and molecular systems to search for time variation of fundamental constants. Our experiment will use molecular vibration spectra to look for changes in the proton-to-electron mass ratio. This thesis discusses our current progress on driving two-photon vibrational transitions in O_2^+. I begin by building up the molecular theory to provide calculations of anticipated transition rates. Next, I give a detailed description of our experimental apparatus and procedure, including updates from the past year which significantly increased our sensitivity. I present recent spectroscopic data in which we did not observe the two-photon transition and estimate possible limits this allows us to place on parameters. I conclude by offering next steps to improve our experiment and make the first experimental observation of this type of transition.

Acknowledgments

I would first like to thank Prof. Hanneke for his support, guidance, and encouragement both in the lab and in the process of composing this thesis. I am especially grateful for his willingness to take me on as a first-year and for teaching me the ropes of AMO physics, a subfield I have grown to love over the past four years.

Thank you to the students who have come before me in the lab, including Annika Lunstad, Boran Kuzhan, and Julia Pfatteicher, whose work I built on and interacted with frequently. I also want to thank Jim Kubasek for helping me build parts in the machine shop and always being a cheerful, encouraging presence.

To Sophie and Sam, I could not have made it through the physics major without you! You continue to inspire me and I wish you the best as our paths diverge.

To the students in Spectra and the people on the CCC, thank you for all of the necessary and amazing DEI work you have accomplished. This department reaps the rewards of your efforts.

Lastly, I would like to thank my friends and family for supporting me through the good times and the bad throughout my time at Amherst.

This thesis is based upon work supported by the Amherst College Provost and Dean of the Faculty and by the National Science Foundation under grant PHY-1806223 (RUI). Additional support came from the Clare Boothe Luce Program of the Henry Luce Foundation.

Contents

List of Figures

Chapter 1

Introduction

1.1 Tabletop physics

Physics research today is exceedingly varied in scope, including quantum devices, emergent properties of many-body systems, living and soft matter, and environmental sensing. In addition to these ever-expanding and relevant topics, fundamental physics research remains a main point of interest.

1.1.1 A problem in fundamental physics

The standard model (SM) is often hailed as the greatest achievement of physics. This is a well-earned reputation, as the standard model's mathematical predictions have led to the discovery of many new particles. Most recently, in 2012, the detection of the Higgs boson at the LHC filled out the palette of SM particles and allowed for further calculations to verify SM predictions [1]. In the low-energy regime, the SM also does exceedingly well. Theoretical calculations and experimental observations of the electron and muon magnetic moments [2, 3], the electron electric dipole moment[1] [4, 5], the fine structure constant [6], and the Lamb shift in hydrogen [3] (to name a

---

[1] In this case, "observations" means repeated and increasingly precise null measurements.

few) are in agreement to very high precision with the SM and are used to place bounds on theoretical models for new physics beyond the standard model. However, the standard model falls short in at least three major and well-established areas of physics: the SM does not include (1) gravity, (2) dark matter or dark energy, or (3) a reason for the matter-antimatter asymmetry in the universe. In order to explain these phenomena, new particles and forces are needed.

For many years collider physics, astrophysics, and precision measurement have worked together as a "three-legged stool" of fundamental physics research [7]. However, we are past the heyday of large accelerators and rapid discoveries that occurred in the second half of the twentieth century. In fact, the Higgs boson is the only new SM particle which has been discovered by an accelerator in the past 20 years, and a popular candidate for dark matter, weakly interacting massive particles (WIMPs), have yet to be detected by particle accelerators or large cold liquid detectors [8, 9]. The lack of a WIMP detection combined with the enormous operating costs of high-energy experiments has fostered renewed excitement about ultralight dark matter candidates and the low-energy, table-top experiments which perform this type of search.

1.1.2 Precision measurement and tabletop physics

Atomic, molecular, and optical (AMO) physics is a subfield of physics which utilizes advances in laser technology to control atomic and molecular systems on the quantum level. The the tabletop size of AMO experiments allow for fundamental physics questions to be probed in a single lab, without relying on distant instruments or large collaborations. This means that many diverse but synergistic experiments are being built and run by small teams to look in different ways for new physics (e.g. [10–13]). These types of low-energy experiments are able to produce results of similar caliber to high-energy physics by leveraging precision measurement.

Precision measurement goes hand-in-hand with precise clocks. Optical atomic clocks, which utilize optical (e.g. laser-reachable) transitions in isolated atoms, are the current standard in metrology [14]. Molecules, with a more complex energy structure than atoms, have transitions with even narrower linewidths. More generally, atomic and molecular spectra are the most accurate frequency references currently in use [15]. The level of precision attainable in measurements of transition frequencies in these systems enables them to be sensitive probes of new physics on energy scales significantly higher than that of the transition [16]. Precision spectroscopy with cold molecules has become a common method of conducting fundamental physics research in AMO physics [17], and is the method we utilize in our experiment.

1.2 Our experiment

Our experiment is attempting to drive a two-photon vibrational transition in O_2^+. O_2^+ is a good choice of molecule because it is homonuclear with spin-0 nuclei. Nuclear symmetry eliminates any internal electric field, which typically gives rise to systematic effects [18]. The spin-0 nuclei additionally constrain the ground electronic state of O_2^+ to have only symmetric rotation states (i.e. those with even parity), which eliminates the possibility of electric-dipole transitions between vibrational and rotational states in the same electronic state (see §1.2.2) and limits the frequencies of the transition spectra to extremely narrow linewidths. This allows our measurement to be limited by the bandwidth of the laser, not the underlying physics we wish to measure.

Intrinsically narrow linewidths make for an exceptional clock. What can we do with a good clock? Metrology is a field in and of itself, but our particular system of choice is sensitive to time variation of the proton-to-electron mass ratio $\mu = m_p/m_e$, which is a fundamental constant. Because the proton, a composite particle, and the electron, an elementary particle, get their mass from different fundamental interactions, their ratio is sensitive to new physics which couples to the electron, Higgs, quarks, or gluons. This includes predicted ultralight scalar dark matter fields or theories for quantum gravity with extra spacial dimensions [19, 20]. Future measurements from our apparatus will constrain these theories,[2] but for now we are still in the phase of preliminary spectroscopy.

1.2.1 Sensitivity to μ

States of a diatomic molecule which involve motions of the nuclei, such as vibrational and rotational states in O_2^+, are states which encode μ. To a first approximation, the diatomic molecule behaves as two masses on a spring with quantized vibrational energy levels. For small v, the molecular potential approximates a harmonic oscillator and the vibrational levels are spaced linearly, as shown in Fig. 1.1 (a). For higher v, the potential becomes anharmonic and approaches the potential of the dissociated atoms, which have no sensitivity to μ. In the regime of linear dependence, the potential is given by

$$V = \frac{1}{2}k(r - r_e)^2, \tag{1.1}$$

where k is the spring constant, r is the internuclear distance, and r_e is the equilibrium distance. The energy eigenstates corresponding to the vibrational quantum number v are [16]

$$E_v = \omega_e \left(v + \frac{1}{2} \right) hc, \tag{1.2}$$

---

[2] Precision measurements searching for deviations in interactions caused by new fields or forces almost always result in a null measurement, which I have heard jokingly referred to as "more precise measurements of zero!" While every physicist hopes to actually make a discovery, most experiments are considered a success if they can put new bounds on a value.

where ω_e is the frequency of vibration in the conventional unit of wavenumbers,[3]

$$\omega_e = \frac{1}{2\pi c}\sqrt{\frac{k}{m}}. \tag{1.3}$$

Here, m is the reduced mass[4] of the two nuclei, which is approximately proportional to the mass of the proton. The spring constant is proportional to the mass of the electron, so we have

$$E_v \propto \omega_e \propto \sqrt{\frac{m_e}{m_p}} \tag{1.4}$$

$$E_v \propto \frac{1}{\sqrt{\mu}}. \tag{1.5}$$

The leading anharmonicity term, which I will not derive here, is

$$-\omega_e x_e \left(v + \frac{1}{2}\right)^2 hc \tag{1.6}$$

and scales as [16]

$$\omega_e x_e \propto \frac{1}{\mu}. \tag{1.7}$$

We also wish to consider the sensitivity of the rotational states, which have energy levels dependent on the rotational quantum number J:

$$E_J = B_e J(J+1)hc = \frac{h^2 J(J+1)}{8\pi^2 I}. \tag{1.8}$$

Here μ couples in via the moment of inertia of the rotating system,

$$I = mr^2. \tag{1.9}$$

---

[3] Note this is not an angular frequency despite the use of ω.

[4] We use m instead of the conventional μ for the reduced mass to avoid confusion with the proton-to-electron mass ratio.

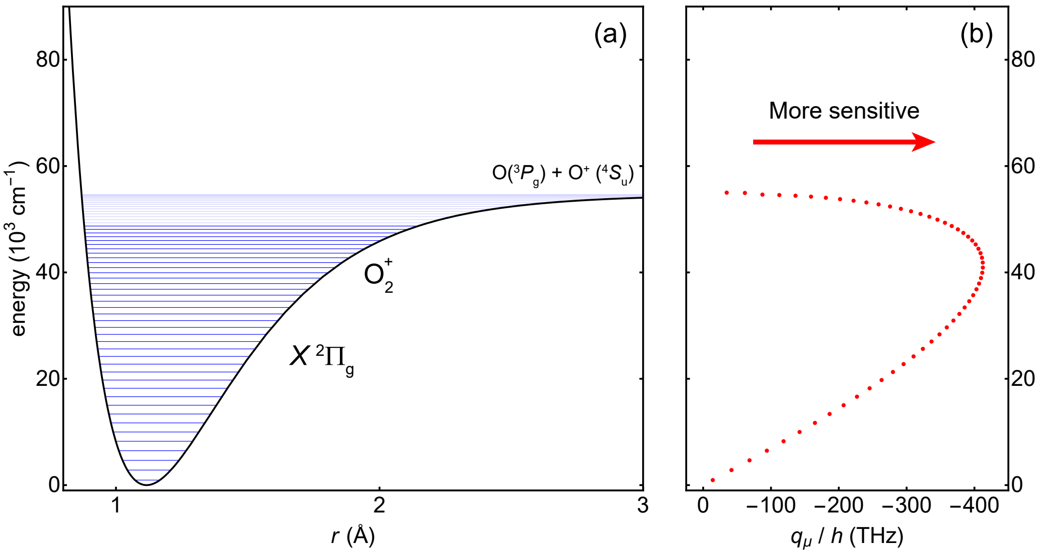

Figure 1.1: Sensitivity of the vibrational levels to μ. (a) shows the potential curve and electronic levels; (b) shows the corresponding sensitivity to μ. Figure from [16] used with permission.

m is again the reduced mass of the two nuclei, proportional to m_p, and $r = r_e$ is the bond length, which relates to the mass of the electron through the spring constant:

$$r^2 \propto \frac{1}{k} \propto \frac{1}{m_e}. \tag{1.10}$$

Thus we have

$$E_J \propto \frac{1}{m_p/m_e} \tag{1.11}$$

$$E_J \propto \frac{1}{\mu}. \tag{1.12}$$

All together, the approximation of the energy of a rigidly rotating anharmonic oscillator[5] with vibrational quantum number v, angular momentum J, and electronic

---

[5] A rigid oscillator sounds contradictory, but I mean to indicate that we have not included effects such as centrifugal distortion from the rotation.

ground state energy T_e is given by

$$E_{v,J} = hc\left[T_e + \omega_e\left(v + \frac{1}{2}\right) - \omega_e x_e\left(v + \frac{1}{2}\right)^2 + B_e J(J+1)\right]. \tag{1.13}$$

We have described the sensitivity of the individual energy levels to μ, but our experiment measures the transition frequency corresponding to the energy change between two states:

$$hf = E'(\mu) - E''(\mu). \tag{1.14}$$

If μ changes over time, then so does the frequency we are monitoring:

$$\frac{\Delta\mu}{\mu} = \frac{\Delta f}{f_\mu}, \tag{1.15}$$

where f_μ is the absolute sensitivity of a transition and is dependent in turn on the absolute sensitivities q'_μ and q''_μ of the states involved [16]. We define f_μ as

$$f_\mu \equiv \mu\frac{\partial f}{\partial\mu} \tag{1.16}$$

$$= \frac{q'_\mu - q''_\mu}{h} \tag{1.17}$$

and q_μ by

$$\Delta E \equiv q_\mu\frac{\Delta\mu}{\mu} \tag{1.18}$$

$$q_\mu = \mu\frac{\partial E}{\partial\mu}. \tag{1.19}$$

Recalling the above scaling relations to μ from Eqs. 1.5, 1.7, and 1.12, we can calculate the absolute sensitivity of a state in our molecule as follows.

$$q_\mu = \mu\frac{\partial}{\partial\mu}hc\left[T_e + \omega_e\left(v+\frac{1}{2}\right) - \omega_e x_e\left(v+\frac{1}{2}\right)^2 + B_e J(J+1)\right] \tag{1.20}$$

$$= \mu hc\Bigg[0 + \left(-\frac{1}{2}\frac{1}{\mu}\right)\omega_e\left(v+\frac{1}{2}\right) - \left(-\frac{1}{\mu}\right)\omega_e x_e\left(v+\frac{1}{2}\right)^2 \tag{1.21}$$

$$+ \left(-\frac{1}{\mu}\right)B_e J(J+1)\Bigg] \tag{1.22}$$

$$= hc\left[-\frac{1}{2}\omega_e\left(v+\frac{1}{2}\right) + \omega_e x_e\left(v+\frac{1}{2}\right)^2 - B_e J(J+1)\right] \tag{1.23}$$

This equation is used to plot the sensitivities of the vibrational levels in Fig. 1.1 (b). The sensitivity peaks at $v = 28$, although the gain in sensitivity is significantly less than linear with v approaching $v = 28$ such that lower vibrational energy levels are reasonable for use in an experiment.

While our experiment utilizes multiple rotational states, transitions between rotational states within a vibrational state are constrained by selection rules to low changes in angular momentum [18]. For this reason we focus on driving a vibrational transition with high Δv.

1.2.2 Two-photon transition theory

As explained in the previous section, we wish to drive a high vibrational overtone $v_X \leq 28$ from our initial state in $v = 0$. The laser frequencies which are easily accessible led us to choose the $|X^2\Pi_g, v = 0\rangle \rightarrow |X^2\Pi_g, v = 16\rangle$ transition from the ground to 16th vibrational state. For an explanation of the molecular term symbol, see §1.2.3; however, for the rest of this section we will use X to abbreviate the $X^2\Pi_g$ potential and v_X to mean the excited vibrational quantum number in the X potential. As mentioned briefly before, vibrational states in the same electronic state of O_2^+ have the same parity. This means that the $|X, v = 0\rangle \rightarrow |X, v_X\rangle$ transition is electric-dipole forbidden. This can be seen clearly by looking at a heuristic[6] for the transition dipole moment:

$$
\begin{aligned}
D_{v_X 0} &= \langle X, v_X | d | X, v = 0 \rangle && (1.24)\\
&= \int_{\text{all space}} \psi^*_{v_X}(\vec{r})\ e\vec{r}\ \psi_0(\vec{r})\ d\vec{r} && (1.25)
\end{aligned}
$$

where the dipole moment $\vec{d} = e\vec{r}$ has a directional quality, so is odd parity. Because $\psi^*_{v_X}(\vec{r})$ and $\psi_0(\vec{r})$ are the same parity, we find the integrand is an odd function and thus the whole integral is zero. With a null transition dipole moment, the transition is forbidden.

What is not forbidden, however, is a transition to a different electronic state. Thus we attempt a two-photon transition through the state $|A^2\Pi_u, v_A\rangle$ (which we will abbreviate as $|A, v_A\rangle$), as shown in Fig 1.2. As an ansatz, one photon drives the transition $|X, v = 0\rangle \rightarrow |A, v_A\rangle$ and the second photon drives the transition $|A, v_A\rangle \rightarrow |X, v_X\rangle$. However, quantum mechanics tells us that we actually drive the transition $|X, v = 0\rangle \rightarrow\rightarrow |X, v_X\rangle$ through all possible excited states $|A, v_A\rangle$. Thus the transition rate, given here as a Rabi frequency in hertz, is a sum over all vibrational states v_A in the electronic state A:

$$
\frac{\Omega_R}{2\pi} = \frac{I}{\epsilon_0 c h^2} \sum_{v_A=0}^{v_A^{(\max)}} \frac{D_{v_A v_X} D_{v_A 0}}{f_{v_A 0} - f_L}, \qquad (1.26)
$$

where I is the intensity of the laser, $D_{v_A v_X}$ is the transition dipole moment between the states $|X, v_X\rangle$ and $|A, v_A\rangle$, $f_{v_A 0}$ is the transition frequency between the X ground state and the A vibrational state, and f_L is the frequency of the laser. On resonance with the vibrational transition, f_L is half the vibrational frequency $f_{v_X 0}$ [18]. Note

---

[6] This equation is a demonstration of the type of integral which defines a transition moment. An actual calculation would involve summing over the positions of all the charged particles in the system. Nonetheless, this sample calculation demonstrates the parity concerns which cause the transition moment to be zero.

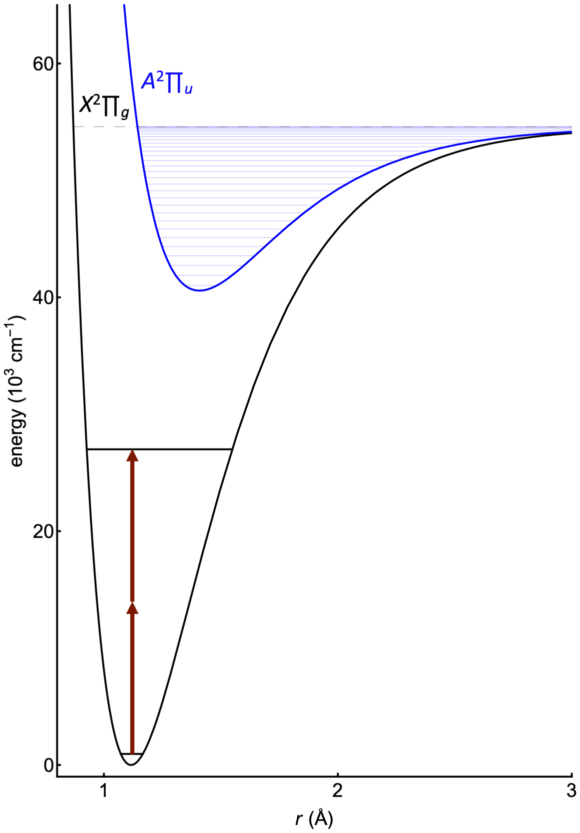

Figure 1.2: Energy diagram of the O_2^+ $|X^2\Pi_g\rangle$ and O_2^+ $|A^2\Pi_u\rangle$ potentials. The two-photon transition is a far off-resonant transition through vibrational states in the O_2^+ $|A^2\Pi_u\rangle$ potential.

that Eq. 1.26 is still an approximation, because it does not include all of the possible electronic and continuum states of O_2^+.

In order to ensure our experimental procedure is tenable, we need to have a high Rabi frequency and thus a high intensity as indicated by Eq. 1.26. Thus we use a pulsed laser to drive the transition, which has pulses 7 ns in duration. When we carry out the Rabi frequency calculation with the parameters of our experiment in Ch. 2, we find a transition time on the order of a nanosecond. Therefore this two-photon transition is a reasonable scheme.

1.2.3 Molecular theory and simulating spectra with PGOPHER

The O_2^+ $|X^2\Pi_g, v=0\rangle \rightarrow O_2^+$ $|X^2\Pi_g, v=16\rangle$ transition has never been driven before (in fact, no two-photon vibrational transition within the same electronic state has been driven before), so we rely on theory and simulation to determine what its spectrum should look like. In particular, we use the physical chemistry software PGOPHER, which is capable of simulating complicated transition spectra from parameters input by the user [21].

Molecular species

Both vibrational states of interest are in the state $|X^2\Pi_g\rangle$ of O_2^+. The X indicates that the molecule is in the ground electronic state, which in this case has even parity (g for *gerade*, *even* in German) as discussed in §1.2.2. Π indicates that the projection of the orbital angular momentum on the internuclear axis is $\Lambda = 1$[7]. The superscript $2 = 2S+1$ indicates that the spin quantum number is $S = \frac{1}{2}$ [23]. All of these parameters are included to define the molecular species in PGOPHER.

For each of the vibrational levels, we also enter the parameters listed in Table 1.1. For a more detailed discussion of the selection of these constants from the literature, see [24].

Initial state preparation

The way in which we prepare the ground vibrational state of O_2^+ determines which rotational states are occupied. In our experiment, O_2 is photoionized with two photons resonantly exciting the Rydberg state of the neutral molecule, O_2 $|d^1\Pi_g\rangle$, and

---

[7] More correctly, $|\Lambda| = 1$. This means there are two possible orientations of the projection of orbital angular momentum on the internuclear axis, $\Lambda = \pm 1$. This results in a splitting in the energy levels known as lambda doubling. In our molecule, the lack of odd parity states causes this to show up as an energy level shift, not a splitting [22].

Parameter	Value, $v = 0$	Value, $v = 16$	Description
T	0	26046.5*	ΔE from the ground state
A	200.289	187.1*	spin-orbit coupling constant
B	1.67996	1.36	rotational constant
D	5.22E-6	-	quartic centrifugal distortion term
p	0.0153	-	lambda doubling constant
q	.00023	-	lambda doubling constant
γ	-.02**	-	spin rotation coupling constant

Table 1.1: Description of parameters used in PGOPHER's simulation [25] and their values for O_2^+ $|X^2\Pi_g, v = 0\rangle$ and $|X^2\Pi_g, v = 16\rangle$. All parameters are given in units of cm^{-1}. *These constants differ from those used in previous simulations [24]. The choice was made to switch to values from [26], which claims a smaller uncertainty than [27]. **This term was not used previously.

one photon ionizing from that state, as shown in Fig. 1.3. We select the rotational angular momentum of the Rydberg state to be $N = 2$ because it has a high transition rate and can populate our desired $J = \frac{1}{2}$ state in the ion. In O_2^+ $|X^2\Pi_g\rangle$, N is not a good quantum number because there is high spin-orbit coupling, so instead we describe the angular momentum of the ionized state by the total angular momentum quantum number J and the projection of the total electronic angular momentum onto the internuclear axis, Ω. The selection rules for which ΔJ are allowed and thus which pairs of J, Ω are occupied are as follows.

ΔJ can be affected by either the photon hitting the molecule or the photoelectron[8] which leaves the molecule. The net orbital angular momentum k imparted on the molecule is

$$k = l \pm 1, \tag{1.27}$$

where l is the orbital angular momentum of the photoelectron (constrained by selection rules for $g \leftrightarrow g$ transitions to be odd) and the 1 corresponds to the photon's

---

[8] A photoelectron is an electron removed from an atom or molecule by a photon. Here, it is the electron which creates the ion O_2^+ from O_2.

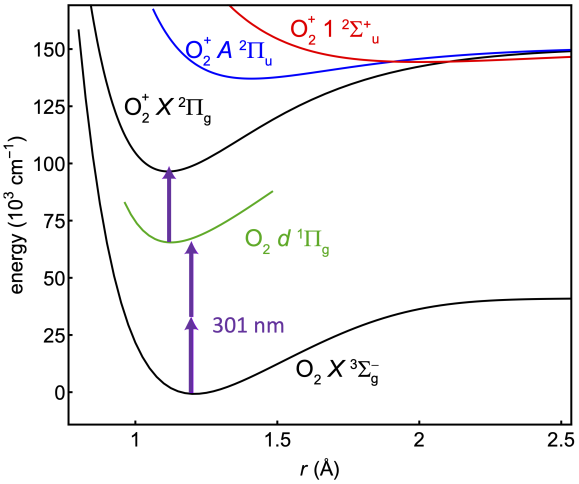

Figure 1.3: State preparation of O_2^+ $|X^2\Pi_g, v = 0\rangle$ through the Rydberg state O_2 $|d^1\Pi_g\rangle$. Figure from [18] used under the Creative Commons license.

spin [18]. The photoelectron also has spin-$\frac{1}{2}$ to contribute, so the total angular momentum imparted is

$$u = \left|k \pm \frac{1}{2}\right| \tag{1.28}$$

with ΔJ taking values $|\Delta J| \leq u$. This gives

$$\Delta J \in \left\{\pm\frac{1}{2}\right\} \qquad (k = 0) \tag{1.29}$$

$$\Delta J \in \left\{\pm\frac{1}{2}, \pm\frac{3}{2}, \pm\frac{5}{2}\right\} \qquad (k = 2). \tag{1.30}$$

Transitions with $k > 2$ contribute minimally to the rotational distribution of the molecules, so we will not consider them here [18].

With $N = 2$ in the Rydberg state, in the molecular ion the states

$$J \in \left\{\frac{3}{2}, \frac{5}{2}\right\} \qquad (k = 0) \tag{1.31}$$

$$J \in \left\{\frac{1}{2}, \frac{3}{2}, \frac{5}{2}, \frac{7}{2}, \frac{9}{2}\right\} \qquad (k = 2) \tag{1.32}$$

can be reached, with the actual J states being a superposition of the corresponding k values. We input $J_{\text{min}} = 0.5$, and $J_{\text{max}} = 4.5$ to PGOPHER for the ground vibrational state.

Because the ionized molecule is a doublet state (the 2 in $|X^2\Pi_g\rangle$), there is an energy splitting of these J states based on the projection of the electron's total angular momentum on the internuclear axis Ω, given by

$$\Omega = \Lambda + \Sigma, \tag{1.33}$$

where $\Lambda = 1$ and $\Sigma = \pm\frac{1}{2}$ are the projection of the electron's orbital and spin angular momentum on the internuclear axis, respectively. Thus we have

$$\Omega \in \left\{\frac{1}{2}, \frac{3}{2}\right\}, \tag{1.34}$$

where Ω can be either of these values for all J except $J = \frac{1}{2}$, where it must be that $\Omega = \frac{1}{2}$. The energies of all the possible states are shown in Fig. 1.4.

Transition selection rules

The accessible J and Ω states in the $|X, v = 16\rangle$ state shown in 1.4 are determined through conservation of angular momentum, which applies to J (but not Ω). In the two-photon transition, each photon has spin-1 which can contribute to J. Together, the two photons create the rule $\Delta J \in \{0, \pm 2\}$.

The last piece of information PGOPHER needs to run the simulation of the transition spectrum is the spherical transition moment for multi-photon transitions, which is given in spherical tensor notation as T(rank, component). Because we have a two-photon transition from a Π state to a Π state, there are three spherical transition moments: T(0,0), T(2,0), and T(2,2) [25]. Together with the constants above and the spherical transition moments, PGOPHER calculates the energy of each level in cm^{-1}

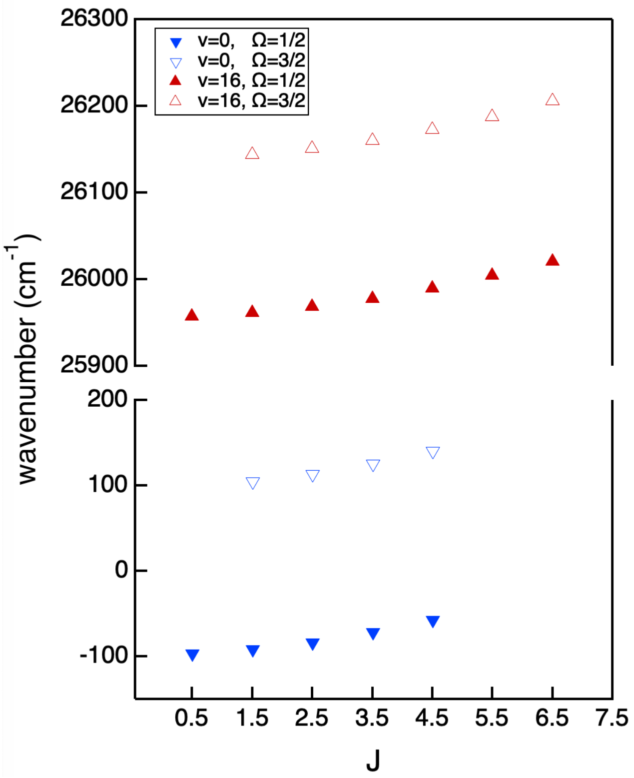

Figure 1.4: Rotational and vibrational energy levels accessible in our system. J is the total angular momentum quantum number and Ω is the projection of the electron's total angular momentum on the internuclear axis.

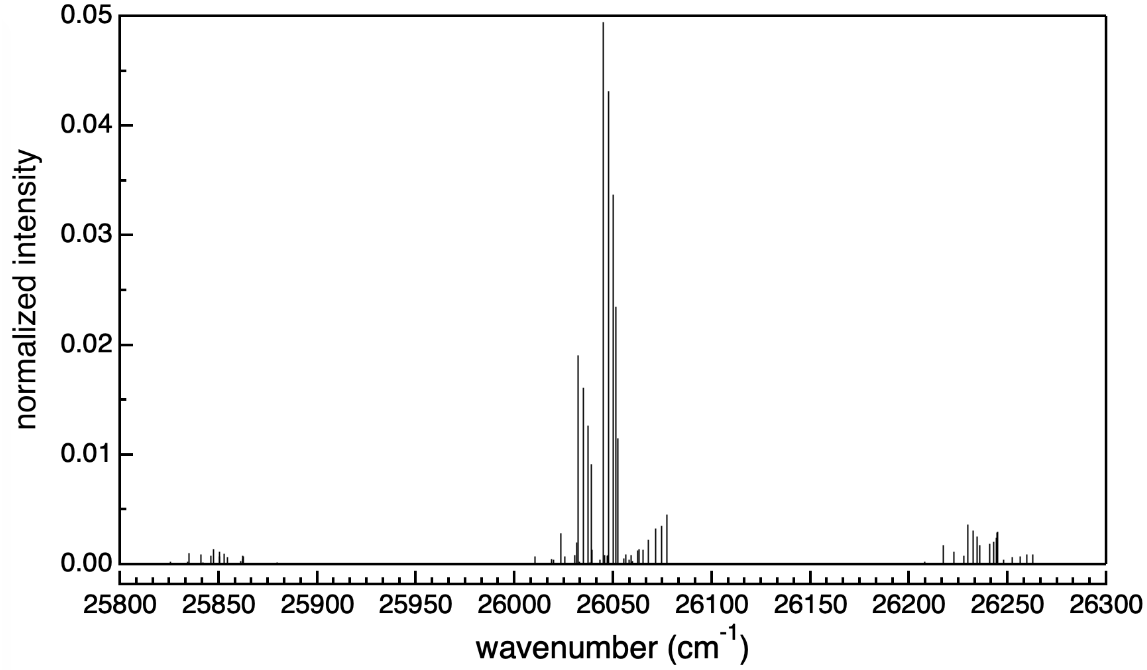

Figure 1.5: Simulation of the $|X^2\Pi_g, v = 0\rangle \rightarrow |X^2\Pi_g, v = 16\rangle$ transition spectrum of O_2^+. Note that because the transition is a two-photon transition, the corresponding laser wavenumber is half the transition wavenumber.

and the transition moments between each level. It outputs a list of all the transition frequencies and their relative intensities, which are plotted in Fig. 1.5.

The outer two lobes consist of the T(2,2) transitions, while the T(0,0) transitions form the tall features in the center lobe and the T(2,0) transitions form the short features in the center lobe. The relative prominence of the features is likely not accurate, as we did not calculate the proper weight for each spherical transition moment. In general, the purpose of the simulation is to find the relative positions of the lines. The uncertainty in the absolute positions is a few cm^{-1}, which arises from prior experiments with single-photon ionization of the neutral molecule [26, 27]. Our experiment aims to measure the absolute position of the transition spectrum precisely, and this measurement will be the first experimental measurement of an electric-dipole forbidden two-photon transition in molecular vibrations.

Chapter 2

Experimental Apparatus and Procedure

This chapter walks through each of the main steps in the experimental procedure and gives the relevant details which allow precise control and measurement of our system. Here we discuss the molecular beam spectroscopy experiment, although in the future the molecules will be confined in an ion trap for longer probing times.

2.1 Overview

Our experiment is a multi-step process through which we measure the success rate of driving the 16th vibrational overtone in O_2^+ $|X^2\Pi_g\rangle$ from the ground vibrational state over a range of wavelengths. A block diagram of the procedure including the pulse chain and resultant transitions is shown in Fig. 2.1, and a cross-section of the experimental apparatus is given in Fig. 2.2.

Following along with Fig. 2.1, the original molecular species is O_2. It is then ionized and state-prepared by a ultraviolet pulse into the ground electronic and vibrational state of O_2^+, $|X^2\Pi_g, v = 0\rangle$. At this point we attempt to drive our target transition $|X, v = 0\rangle \rightarrow |X, v = 16\rangle$ to the 16th vibrational overtone. We detect the

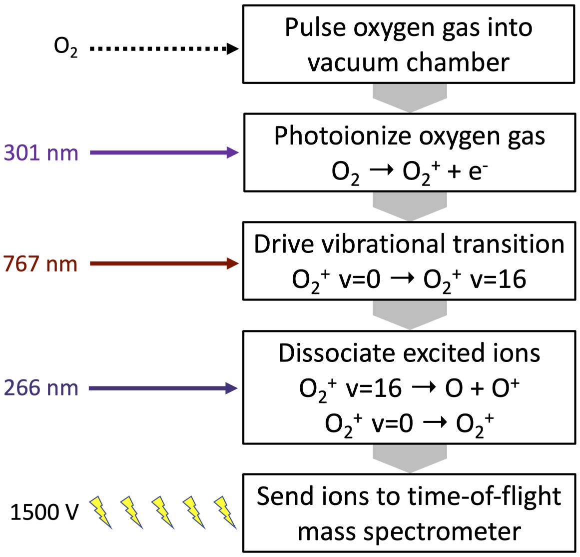

Figure 2.1: Block diagram of the experimental procedure.

success rate of this transition by dissociating the excited ions selectively and utilizing a time-of-flight mass spectrometer.

2.2 Molecular beam

We begin with a canister of O_2, which is sent through a teflon tube to the vacuum chamber. Before allowing any gas to enter the chamber, we purge the line with a simple valve. When the experiment is running, we pulse the gas into the antechamber through the gas valve as seen in Fig. 2.2. The gas trigger lasts 130 µs and the voltage on the poppet is set to 400 V. The molecular beam then passes through a skimmer, which removes the outer part of the beam and only keeps the inner, cool gas. Expanding into the main chamber, the beam expands supersonically and cools further to an estimated temperature of 20 K, followed by a 300 K thermalized tail [28].

After traveling 142 mm, the gas beam is in the center of the experiment zone and has a diameter of 1.4 mm [24]. It is in the experiment zone where the molecular beam is hit with a rapid series of laser pulses taking a total of 24.5 ns. The molecular beam travels at 739 m/s and thus in this time, the gas molecules move 18.1 µm.

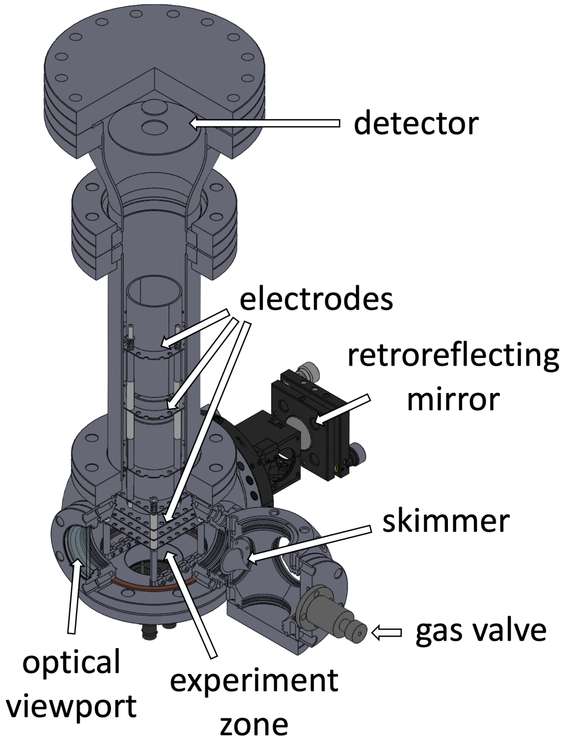

Figure 2.2: The experimental apparatus. As a scale indicator, the circular flange at the top has a 6 in diameter.

2.3 Ionization

The ionization scheme is $2+1$ resonance-enhanced multi-photon ionization (REMPI) using a 301 nm pulse. This light originates from an InnoLas SpitLight 600-10Hz Nd:YAG pulsed laser outputting a 532 nm (internally frequency-doubled from 1064 nm) beam 6 mm in diameter with a pulse duration of 6–7 ns. This pumps a Quantel TDL-60 dye laser (call this the REMPI dye laser) with a mixture of Rhodamine 610 and Rhodamine 640 dye to produce 602 nm light[1]. We then convert to 301 nm via second harmonic generation (SHG) in a nonlinear crystal. For a discussion of this process, see Appx. A.

We found that for increasing the ionization rate of O_2 (after we found the correct resonance by scanning the REMPI spectrum), the single most important factor was intensity at the focus. This was most easily affected by increasing the pulse energy,

---

[1] See [28] for a discussion of this wavelength selection

which we accomplished with several changes in the beamline.

First, we switched the SHG crystal from KD*P to a newer β-Barium Borate (BBO) crystal, which has a higher conversion efficiency. The conversion efficiency depends on a parameter d_{eff} of the crystal as well as the electric field intensity in the crystal and its walk-off, since the 602 nm and 301 nm light have different indices of refraction. For KD*P, $d_{\text{eff}} = 0.365$ pm/V and for BBO, $d_{\text{eff}} = 1.88$ pm/V, which is a factor of 5 improvement. The walk-off in BBO is higher (82.15 mrad as opposed to 23.66 mrad in KD*P), which means we must use a much shorter crystal length (7 mm as opposed to 35 mm), so do not quite get a factor of 5 improvement. We also adjusted the telescope focusing into the lens for a tighter focus. With these changes, we increased the REMPI energy from 1 mJ to 2.2 mJ. Additional considerations in the installation had to be taken to allow scanning of the REMPI spectrum; these are discussed in Appx. A.

Second, the old Quantel YG660 Nd:YAG pump laser was having stability issues and was low in energy, so we exchanged the pump light for the InnoLas Nd:YAG, which also pumps the transition laser. This was achieved by installing a 70/30 beamsplitter in the 532 nm output and directing the smaller beam to the REMPI dye laser. The end result was an increase from 5.2 mJ to 11.1 mJ output in the 601 nm light. A side effect of pumping both dye lasers from the same Nd:YAG (in addition to the dissociation beam coming from the 1064 nm light frequency-quadrupled to 266 nm) is that we had to optically delay the pulses instead of creating the pulse timing electronically. The resultant timing is described in Table 2.1.

The number of shots which produced molecular ions before these changes was 30–80%, while now we can routinely peak up to 98–100% ion generation by readjusting the BBO crystal, with the actual number of ions (determined by the integral of the O_2^+ trace) an even better improvement than indicated by the percent of shots producing ions.

	Arrival time in ns	
Laser	from start	from previous
REMPI	396.5	
transition	404.7	8.2
dissociation	414.0	9.3

Table 2.1: Timing of the pulse chain. “From start” means time since the main experiment trigger and “from previous” means time since the beginning of the previous laser pulse. The pulses are 7 ns long, so we aimed for “from previous” times $\gtrsim 7$ ns.

2.4 Two-photon transition

2.4.1 Transition laser

To drive the main transition we use an infrared (≈ 767 nm) pulse. The beam is from a Sirah Cobra Stretch dye laser (call this the transition dye laser) with Styryl 8 dye (also known as LDS-751) pumped by the same 532 nm output of the Nd:YAG laser as the REMPI beam. The pulse duration is 7 ns and before the lens which focuses the pulse into the vacuum chamber, it is 20.5 mJ in strength. This gives a power P of 2.9 MW. The radius ω_1 of the beam entering the lens is 2.5 mm, while the lens itself has a focal length F of 100 mm. Assuming a Gaussian beam profile[2] and diffraction-limited optics[3], the beam waist at the focus is

$$\omega_0 = \frac{\lambda F}{\pi \omega_1} \tag{2.1}$$

$$= 9.8\ \mu\text{m}. \tag{2.2}$$

Because our beam shape is definitely not a smooth Gaussian, this is a good order of magnitude estimate, but the actual waist is likely a few times larger.

The pulse is retroreflected back through the chamber after its first pass by a

---

[2] Our beam shape is quite far from a Gaussian in appearance, but should behave similarly at its center.

[3] This is true for our achromatic lens, but the beam is also diffracted slightly when entering the vacuum chamber through the window.

spherical mirror as seen in Fig. 2.2, preserving the point of focus. This is a key step, as having photons intersect the molecular beam from both sides mean that the first-order Doppler shift in energy seen by molecules with lateral motion is cancelled [28]. Because the transition laser could be damaged by sending the beam back into it, we include an optical isolator in the beam path shortly after the beam exits the transition laser port.

2.4.2 Transition rate calculation

As discussed in §1.2.2, the Rabi frequency must be high enough such that the transition has a reasonable probability of occurring on the timescale of the laser pulse. Eq. 1.26 indicates that Ω_R depends linearly on the intensity of the laser, which is power per unit area. The power of the electric field is almost doubled by the retroreflection of the beam, but not quite. The back vacuum window is calcium fluoride (CaF_2) with a reflectivity of 3.14% at 767 nm. Passing through four surfaces of the window on its path, the power of the retroreflected beam is 88% of what is was on its first pass through the chamber. Thus the total intensity at the focus is given by

$$\begin{aligned} I &= \frac{1.88P}{\pi\omega_0^2} && (2.3) \\ &= \frac{1.88(2.9 \times 10^6 \text{ W})}{\pi(9.8 \text{ µm})^2} && (2.4) \\ &= 1.8 \times 10^{16} \text{ W/m}^2. && (2.5) \end{aligned}$$

From Table 1 in [18], we have that for the $|X, v = 0\rangle \rightarrow |X, v = 16\rangle$ transition,

$$\frac{\Omega_R}{2\pi I} = 0.96 \times 10^{-7} \frac{\text{Hz}}{\text{W/m}^2}. \quad (2.6)$$

Thus we have a calculated transition time of

$$\frac{\pi}{\Omega_R} = 0.28 \text{ ns} \tag{2.7}$$

and can expect to drive this two-photon transition with our lasers.

One additional consideration is the motion of the molecular ions during the pulse chain. Using the times from Table 2.1 and the molecular beam speed of 739 m/s, we can calculate that the ions move 11.2 µm from the beginning of the ionization pulse to the end of the transition pulse, which is a significant fraction of the 19.6 µm waist diameter we claim above and would eat into our signal significantly. While this is not ideal, there are multiple factors which mitigate this effect. First, as explained in §2.4.1, our beam waist calculation is likely underestimating the size of the beam focus by at least a factor of 2. Second, the gas beam is 1.4 mm in diameter, which is large enough to encompass the Rayleigh range (i.e. the distance from center in which the beam radius is larger by a factor of $\sqrt{2}$ than the waist) of the laser beams' foci. This means that even if the ions in the center of the gas beam are moving too quickly to experience both pulses at the waist, there is still an appreciable amount of gas which is off-center from the focus and thus still within the beam for both pulses. Of course, the intensity for the non-focused region is less than that at the focus, which would lead to longer transition times. However, the transition time can be 24 times longer than the base transition time of 0.28 ns before exceeding the pulse duration.

2.5 Dissociation

In order to determine whether the vibrational transition was successfully driven, we pulse the gas beam with a 266 nm laser. If the O_2^+ is in the excited vibrational state, this pulse has enough energy to dissociate the molecule, as shown in Fig. 2.3. The resulting ratio of O^+ to O_2^+ is then a measure of the success rate of the vibrational

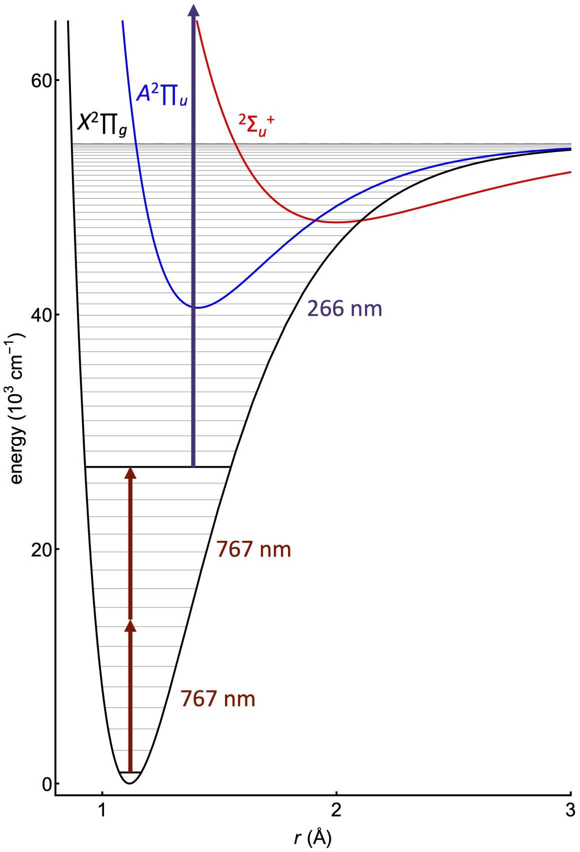

Figure 2.3: Energy diagram of O_2^+. Molecules in the 16th vibrational state can be photodissociated with 266 nm light.

transition.

One area of concern is that the theory calculations for the dissociation cross sections of different energy levels have some uncertainty in the frequency domain. Because the dissociation functions have rapid changes in cross section for small frequency shifts, as seen in Fig. 2.4, the actual dissociation probability for a given vibrational overtone and dissociation laser has a high uncertainty. Thus the dissociation cross section of the 16th vibrational level and 266 nm light may be significantly lower than expected. For this reason it may be necessary to try dissociating with 355 nm instead (1064 nm tripled) or switching to a different vibrational state altogether.

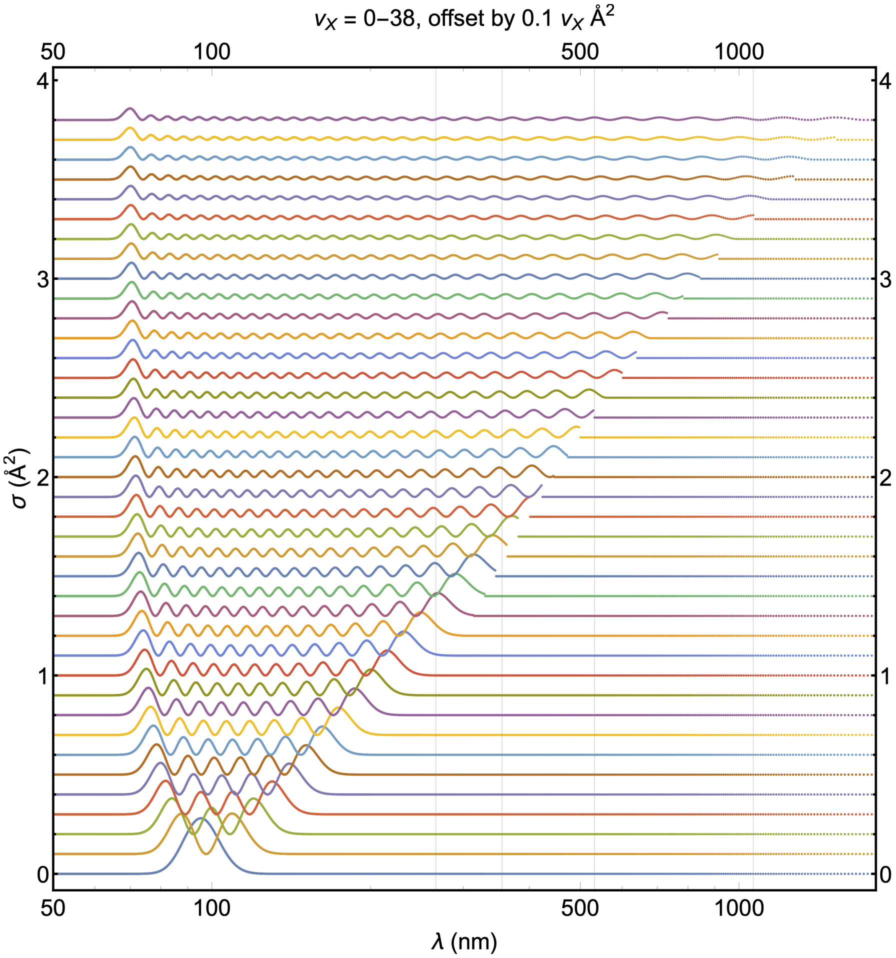

Figure 2.4: Theoretical dissociation cross sections of the $v = 0$ to $v = 38$ vibrational levels in O_2^+ $|X^2\Pi_g\rangle$. The levels are vertically offset by .1 $\mathring{A}^2$ such that the $v = 0$ level is the bottom curve. Note that discontinuities occur at the threshold photon energy (and corresponding wavelength) for dissociation of each level. The vertical gray lines are at 266, 355, 532, and 1064 nm, respectively.

2.6 Mass spectrometry

To determine the ratio of O^+ to O_2^+ after dissociation, we pulse on electrodes on either side of the experiment zone to send the ions up a time-of-flight mass spectrometer (TOFMS). Because O^+ and O_2^+ have the same energy but masses different by a factor of two, when they are accelerated through the same potential, the resulting arrival times are scaled by a factor of $\sqrt{2}$:

$$\frac{1}{2}m_{16}v_{16}^2 = \frac{1}{2}m_{32}v_{32}^2 \tag{2.8}$$

$$m_{16}\left(\frac{d}{t_{16}}\right)^2 = m_{32}\left(\frac{d}{t_{32}}\right)^2 \tag{2.9}$$

$$\left(\frac{t_{32}}{t_{16}}\right)^2 = \frac{m_{32}}{m_{16}} \tag{2.10}$$

$$\frac{t_{32}}{t_{16}} = \sqrt{2}. \tag{2.11}$$

When an ion hits the micro-channel-plate charged particle detector (MCP) at the top of the TOFMS, it causes a shower of electrons to fly off. These electrons form a current pulse that then gets changed into a voltage dip over some small time scale (on the order of a nanosecond) and recorded by a high-speed oscilloscope. The time difference corresponding to our mass scales is easily resolved, as demonstrated by Fig. 2.5. While we claim the dip at $m = 16$ is O^+, the TOFMS only distinguishes charge-to-mass ratios and thus any O_2^{2+} would appear at the same time. However, it is reasonable to expect that we would dissociate O_2^+ before doubly ionizing it the vast majority of the time.

In order to utilize the TOFMS signal, we must calibrate the t_0 offset (not $t = 0$, i.e. the experiment trigger time, but the time when $m = 0$) marked on the mass axis of Fig. 2.5. This should occur when the electrodes turn on, but even with the fast voltage ramp, the ions experience the ramping time. Thus we back-calculate the effective t_0 by recording t_{32} and t_{16}. The REMPI pulse provides a reliable source

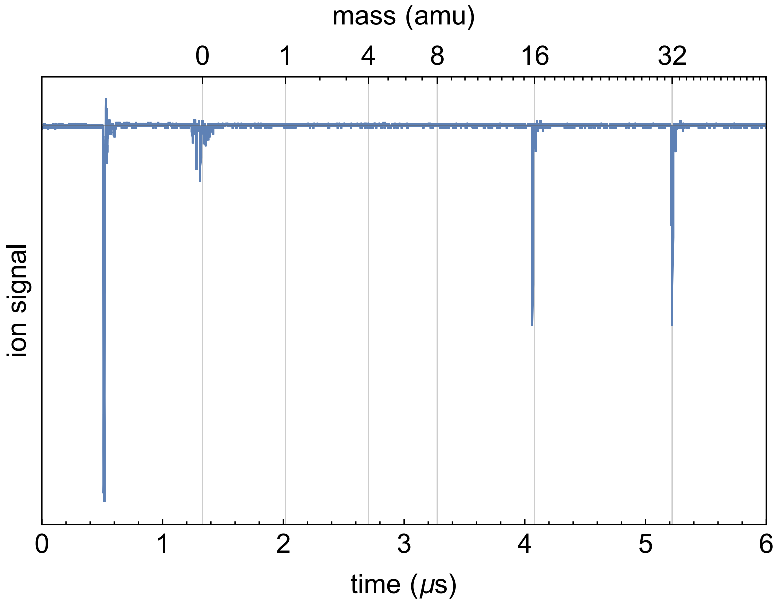

Figure 2.5: Demonstration of the TOFMS signal as a function of time since the experiment trigger. The first dip is the laser pulses and the second dip is the electrodes turning on; this sets our approximate 0 mass. The following two dips are the O^+ and O_2^+ signals, respectively. Note that the mass scaling assumes a singly charged ion; doubly charged ions would appear at half their mass.

of O_2^+, and a higher power of the dissociation pulse than used when running the experiment produces visible quantities of O^+. Using cursors on the front panel of a LabView program, as shown in Fig. 2.6, we found that $t_{32} = 5.22$ µs and $t_{16} = 4.07$ µs, giving $t_0 = 1.33$ µs.

The electrodes themselves are arranged as shown in Fig. 2.7 with voltages as described in Table 2.2. Electrodes 1–3 are in a Wiley-McLaren configuration and control the initial acceleration of the ions out of the experiment zone, which lies between electrodes 1 and 2. Electrodes 2 and 3 are made out of a fine mesh grid that allows the ions to pass through while maintaining a uniform potential. Electrodes 4–6 form an einzel lens, which focuses the ions onto the MCP. While this focusing in theory affects the charge-to-mass timing calibration of the TOFMS, no significant deviation from the $\sqrt{\frac{m_2}{m_1}}$ ratio was found in simulations done when designing the electrode structure of our system [24].

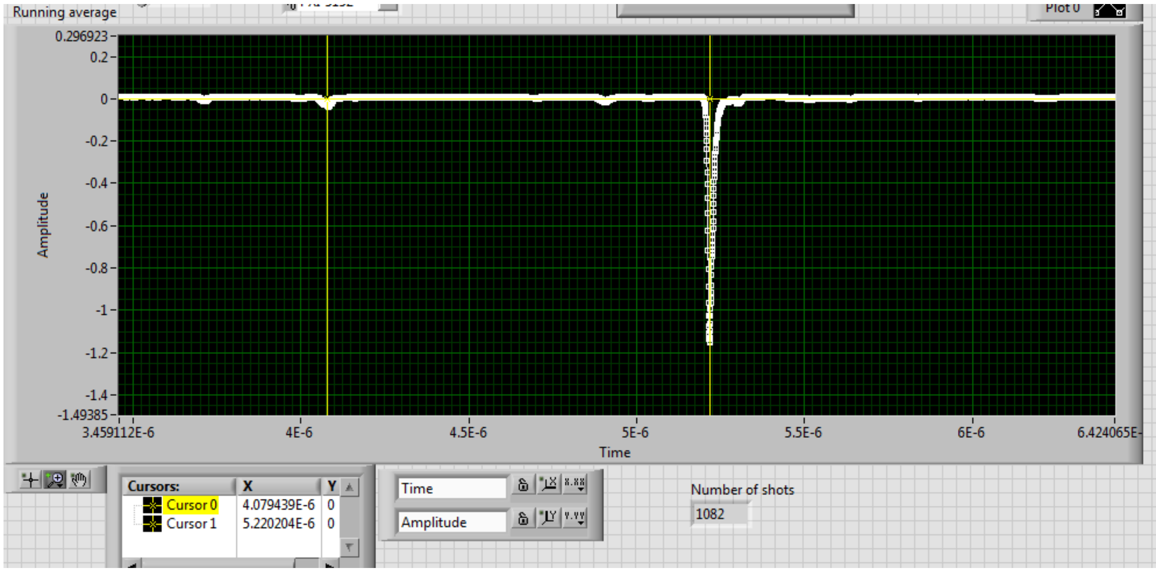

Cursors:	X	Y
Cursor 0	4.079439E-6	0
Cursor 1	5.220204E-6	0

Number of shots: 1082

Figure 2.6: Trace of the MCP signal on the TOFMS with cursors marking the times t_{16} and t_{32}.

Wiley-McLaren Electrodes			Einzel Lens Electrodes		
1	push	1730 V	4	bottom	0 V
2	grid	1500 V	5	center	1600 V
3	top	0 V	6	top	0 V

Table 2.2: Electrode voltages, as numbered in Fig. 2.7. The MCP voltage is -2980 V, although this is screened by 0 V so it does not affect the free flight path of the ions in the TOFMS.

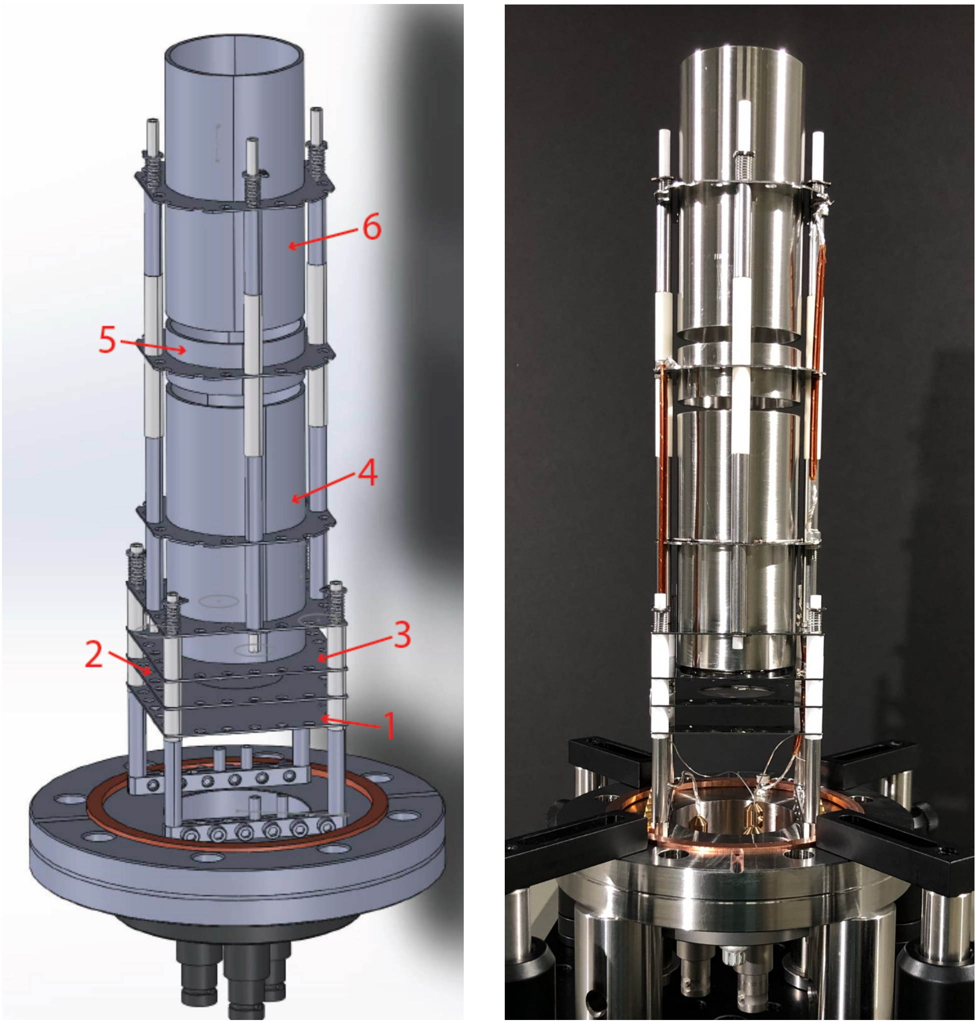

Figure 2.7: CAD render (left) courtesy of Boran Kuzhan [24] and photo prior to installation (right) of the Wiley-McLaren and einzel lens electrodes in the TOFMS. Note that 1, 2, and 3 are planar, while 4, 5, and 6 are tubular. Electrodes 4 and 6 are 3.00 inches long [24].

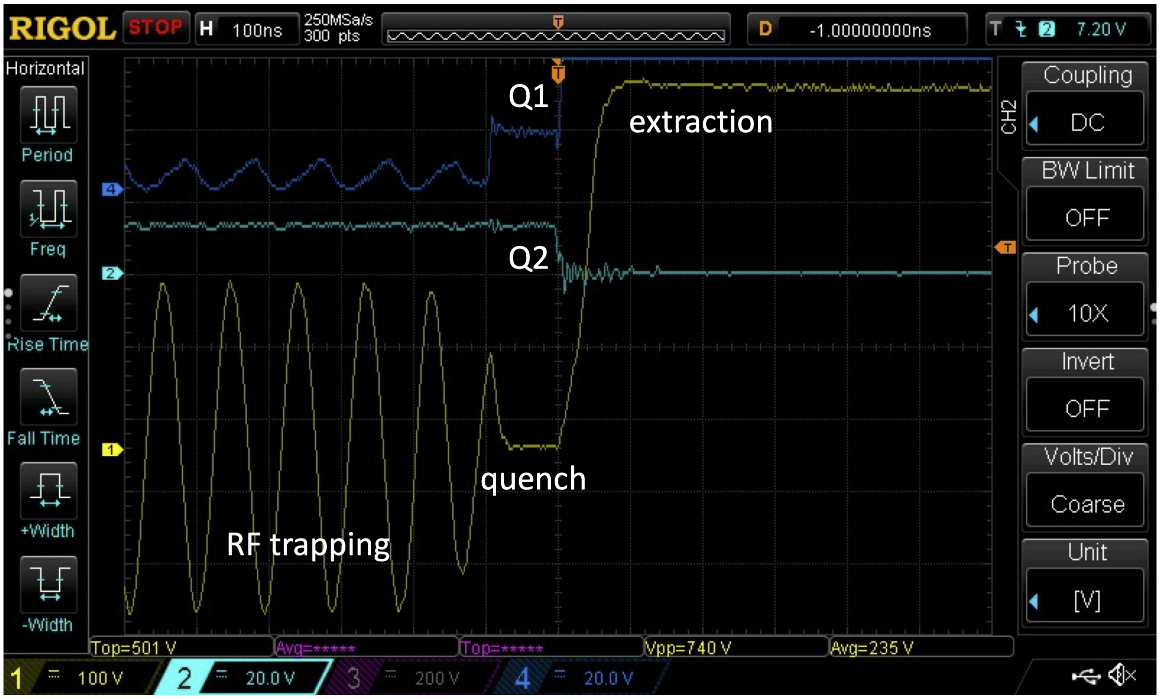

Figure 2.8: Oscilloscope trace of the response of the extraction circuit to each of the triggers. Q1 is the logic signal to a transistor which initiates the quench of the trapping voltage and Q2 is the logic signal to initiate the extraction voltages, which are currently attached to the Wiley-McLaren electrodes.

2.6.1 Pulsing electronics

To ensure that the three laser pulses, which span 24.5 ns, all hit the gas molecules before they are accelerated upwards, the experiment is carried out in zero-field. After the pulse chain is complete, but before the gas has traveled too far (experimentally optimized to be 1 µs after the main experiment trigger [28]), the electrodes are pulsed on to accelerate the ions into the TOFMS and are held at high voltage for 200 µs. The pulsing electronics which let us turn on upwards of 1 kV in ≈ 100 ns are part of the ion trap voltage control circuit designed by Julia Pfatteicher [29] and optimized by me for the quick application of the high TOFMS pulse voltages. Fig. 2.8 demonstrates the ability of the circuit to switch between an RF trapping voltage (not currently in use) and a high extraction voltage. The rise time of a 500 V extraction voltage from its trigger is < 100 ns.

Instance	Description	Bin center (μs)	Bin width (μs)
0	O_2^+	5.25	.400
1	O^+ narrow	4.07	.200
2	O^+ medium	4.07	.400
3	O^+ wide	4.07	1.00
4	mystery (39–44 amu)	5.72	.400
5	control (14 amu)	3.87	.200
6	control (18 amu)	4.22	.200

Table 2.3: Data instances and corresponding time bins. We track three widths of the O^+ signal as well as the molecular ion signal, two control windows, and a "mystery signal" which is a particularly active and wide band in our TOFMS signal with an unknown source.

Even with the einzel lens focusing the arrival times for ions of the same species, there is a rise time associated with the voltage pulse given off by the MCP to indicate a signal. We record as data the integral of the MCP trace in a time bin corresponding to the time and width of the various ion species we care about. The values of the time bins we record are given in Table 2.3. This gives us the capability to detect O^+ and O_2^+, the ratio of which gives us our signal. In practice, the O_2^+ production is relatively constant,[4] and we only pay attention to the O^+ signal.

2.7 Scanning

Up until this point I have described how to get a single measurement of O^+. However, we are interested in scanning a range of wavenumbers in the transition laser to look for the transition spectrum of our desired transition, $O_2^+ \ |X^2\Pi_g, v = 0\rangle \rightarrow O_2^+ \ |X^2\Pi_g, v = 16\rangle$.

Our experiment code has inputs for the start wavenumber, end wavenumber, start percentage, step size, and number of shots per step. The start and end wavenumbers

---

[4] The ion production actually decreases by about 5–10% at best over the course of a day, so for multiple day stretches of data-taking we stagger the start of each scan, as described in §2.7.

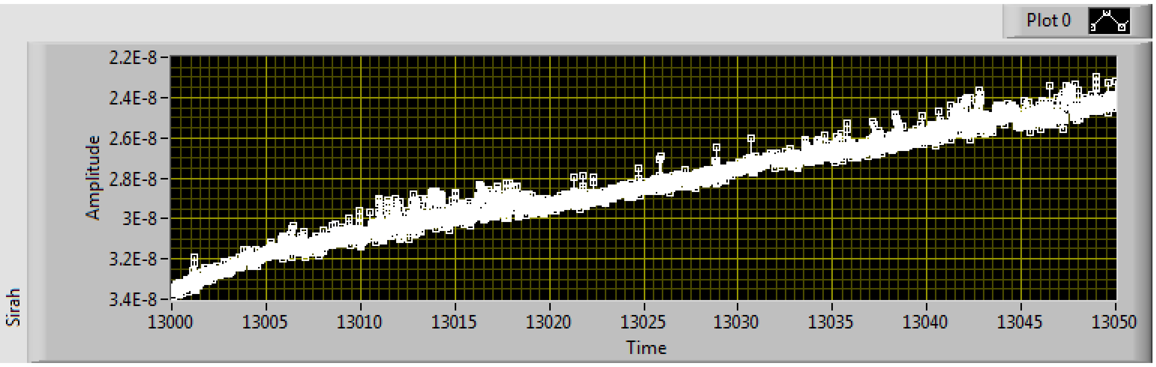

Figure 2.9: Example of decreasing power from the transition dye laser over the course of a full day. Note that the y-axis is flipped and the units of the time axis are given in wavenumber, which is a proxy for time.

determine the range of the scan. For a full data run, we scan the transition laser from 13000 cm^{-1} to 13050 cm^{-1}, which covers the entire middle portion of the simulated spectrum depicted in Fig. 1.5. A buffer of about 10 cm^{-1} on either side of the middle features is also given to account for the few cm^{-1} uncertainty on the location of the transition as well as any inaccuracies in the nominal versus actual wavenumber output by the transition dye laser, as discussed in Appx. B.

The start percentage parameter allows the user to start a scan a certain percentage of the way through the scan range. When the laser reaches the end of the scan range, it will then wrap around to the beginning and continue until every part of the scan range has been covered. The motivation for this option comes from the fact that dye lasers burn through their dye as they run, and the transition dye laser does this appreciably, resulting in a steadily decreasing power over the course of a day as seen in Fig. 2.9. For data runs involving multiple full days of data taking, each day's scan can cover the full range but be started a different fraction of the way through, which helps to eliminate systematic effects.

The step size parameter determines how many cm^{-1} the transition laser increments by with each successive step through the scan range. When trying to see the features of a transition spectrum, it is important to have a step size which allows this

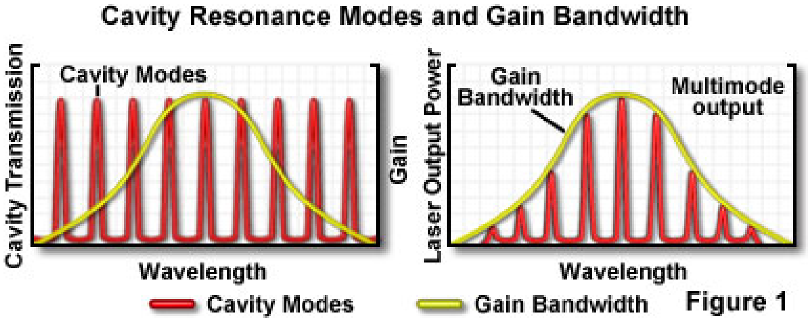

Figure 2.10: Axial modes (also called cavity resonance modes) vs. gain bandwidth in a laser. Figure from [30], used with permission.

level of detail. The linewidth of each transition feature seen in Fig. 1.5 is extremely narrow (sub-hertz), so our scan resolution is limited by the bandwidth of our laser. Unfortunately, the bandwidth of the transition laser set by the diffraction grating, 0.072 cm^{-1}, is only an envelope for multiple frequencies under this envelope corresponding to the various axial modes of the cavity, each with a bandwidth of 0.005 cm^{-1} (set by the pump laser duration). The spacing of these axial modes (set by the cavity length) is 0.017 cm^{-1}, which is large enough that we could miss the linewidth of our transition even if it falls under the envelope of the pulse. A diagram explaining the concept of axial modes is provided in Fig. 2.10.

To combat the effect of the axial modes, we employ the dynamic mode option (DMO) of the transition laser, which dithers a piezo in the cavity to return a smooth frequency distribution within the gain bandwidth. The effect of the DMO as determined by Sirah Lasertechnik is shown in Fig. 2.11, although we do not have a way to reproduce this data.

Once we trust the frequency output of the laser is well represented by a bandwidth of 0.072 cm^{-1}, it is still good to have step sizes smaller than this to ensure a smooth scanning of all possible frequencies in the scan range. We typically use a step size of 0.015 cm^{-1}.

Lastly, the number of shots per step is the number of times at a given wavenumber we run the code to pulse the gas, fire the lasers, and read out the data. We determine

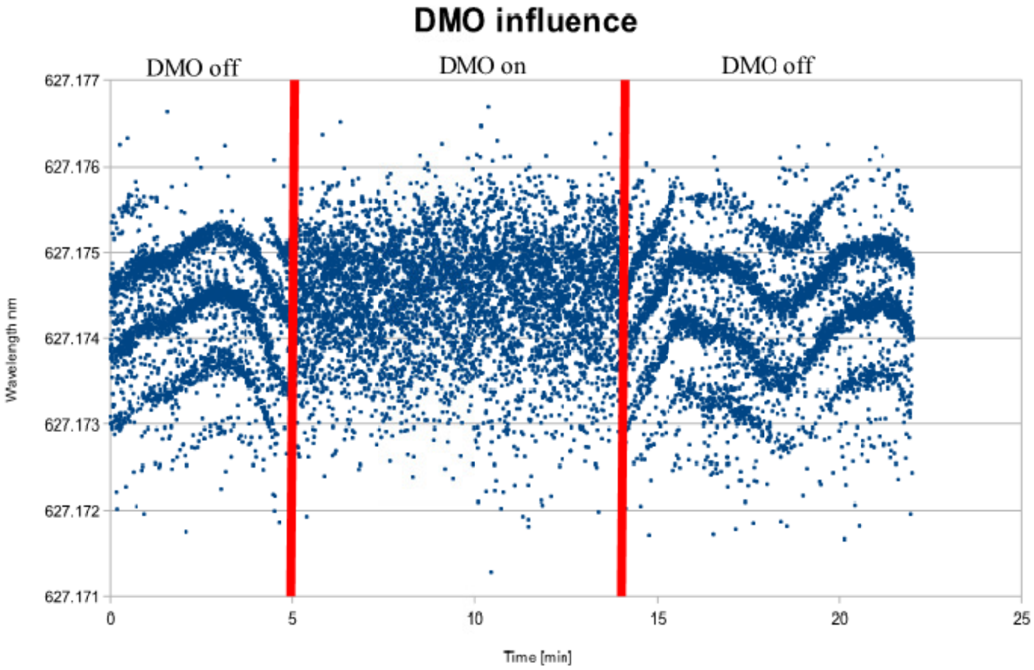

Figure 2.11: Effect of the dynamic mode option on the Sirah pulsed dye laser. Figure courtesy of Paulus Jauernik from Sirah Lasertechnik [31].

this value by the total amount of data we wish to take at each step divided by the number of scans we will be running over the scan range to acquire the data. For purposes of eliminating systematic sources of noise, it would be best to only take one data point per step and randomly choose the wavenumber for each data point within the scan range. However, this is not practical because the stepper motor in the laser always approaches a wavenumber from below to account for backlash in the gears. In addition, each step has a few seconds of overhead from storing data (this overhead increases over the course of a scan) which adds up quickly and is a reason to take a significant number of data points at each step.

Chapter 3

Data and Analysis

3.1 Signal processing

The signal we wish to distinguish is how many ions, and of what type, hit our detector each shot. By averaging over many shots, we hope to increase the potential of seeing a signal if we are at the correct wavelength for a two-photon transition. While we have a good ability to distinguish ion species using time separation, the number of ions making up a given signal is difficult to ascertain. After the MCP changes the incoming ion to a voltage dip, we check if it passes some threshold. If a dip occurs, we integrate it and record the value (in V·ns) in a “raw” data file, which gives a list of each shot and the corresponding ion integral. For most analysis purposes, however, we go one step further and average the integrals corresponding to each step, which is saved in a “processed” data file listing wavenumbers and average ion integrals.

Fig. 3.1 is a histogram showing one scan’s set of ion integrals detected by the MCP in the narrow O^+ time bin. Visually, it is clear there is not a single simple distribution of signal magnitudes, but rather a multi-mode structure under a larger envelope. These smaller maxima no doubt correspond to the discrete number of ions that caused the original electron shower. Counting from the right, the first, second,

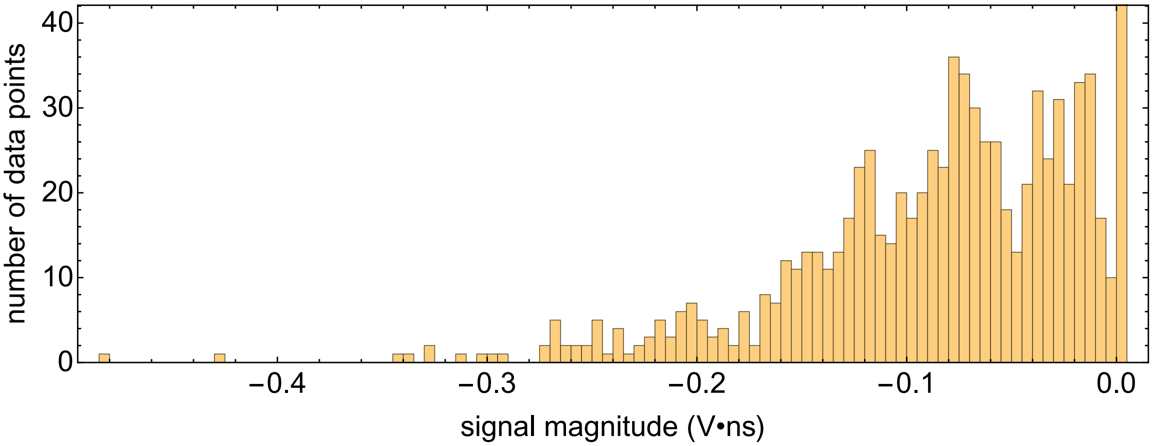

Figure 3.1: Histogram of sample ion data. The discrete nature of the original signal is discernible in the distribution. There are 1,264 points in the 0 bin, as most shots do not produce O^+.

and third peaks are relatively clear. Further to the left it seems as though this multimode structure continues, although it becomes unclear which peaks actually peak where.

Additionally, Fig. 3.1 begs the question of how one should do statistical analysis on this type of data. If we were to fit curves to the histogram, what distribution would they follow? The original events of ions hitting the MCP should follow a Poisson distribution, but a Poisson distribution is a discrete distribution. How then should we describe the continuous nature of the ion integrals?

3.2 A long scan

When it finally seemed the apparatus was ready with good pulse powers, we took our first long data run of the two-photon spectrum. We chose to scan a full 50 cm^{-1}, from 13000 cm^{-1} to 13050 cm^{-1}, which covers the central features in the simulation shown in Fig. 1.5. We also left a margin of about 10 wavenumbers on either side, which, together with the width of the scanning region, we hoped was plenty wide to account for any inaccuracies in the nominal wavenumber[1] as well as the documented uncertainty of a few cm^{-1} of the simulated spectrum. In the (relatively likely) event that we did not see anything in the scan, we wanted to eliminate the possibility that we were not looking in the correct place.

The scan took step sizes of 0.015 cm^{-1}. Because the bandwidth of the transition laser is 0.072 cm^{-1}, this meant that any features of the transition would be roughly 5 steps wide and clearly visible as a signal. We picked the number of shots/step such that each day would have 8 hours of running time. With 7 days of data, a 50 cm^{-1} range, a step size of 0.015 cm^{-1}, and the laser pulsing at 10 Hz, this amounted to 86 shots/step/day for a total of 602 shots/step. Additionally, we staggered the start wavenumbers by $1/7 = 14\%$ a day to minimize drifts in systematic variables such as laser power, temperature, etc. impacting our data disparately at different wavenumbers.

3.2.1 Issues and maintenance

As typical in experimental physics, the data taking process was not as smooth as we had envisioned.

Molecular ion production

The first major issue was that our molecular ion production was much lower than anticipated. Fig. 3.2 shows the molecular ion integral over the course of each day. Most days began with lower ion production which increased over the span of about 5 cm^{-1}, or 45 minutes, and then gradually dropped throughout the day.

While the molecular ion integral does correspond to the general REMPI energy seen in Fig. 3.3, the apparent correlation between the initial ion dip and the initial

---

[1] This was before the new wavemeter arrived, so we were using the nominal wavenumber from the Sirah dye laser as our calibration source. After comparing with the new wavemeter later on, we found the nominal wavenumber is about 5 cm^{-1} off.

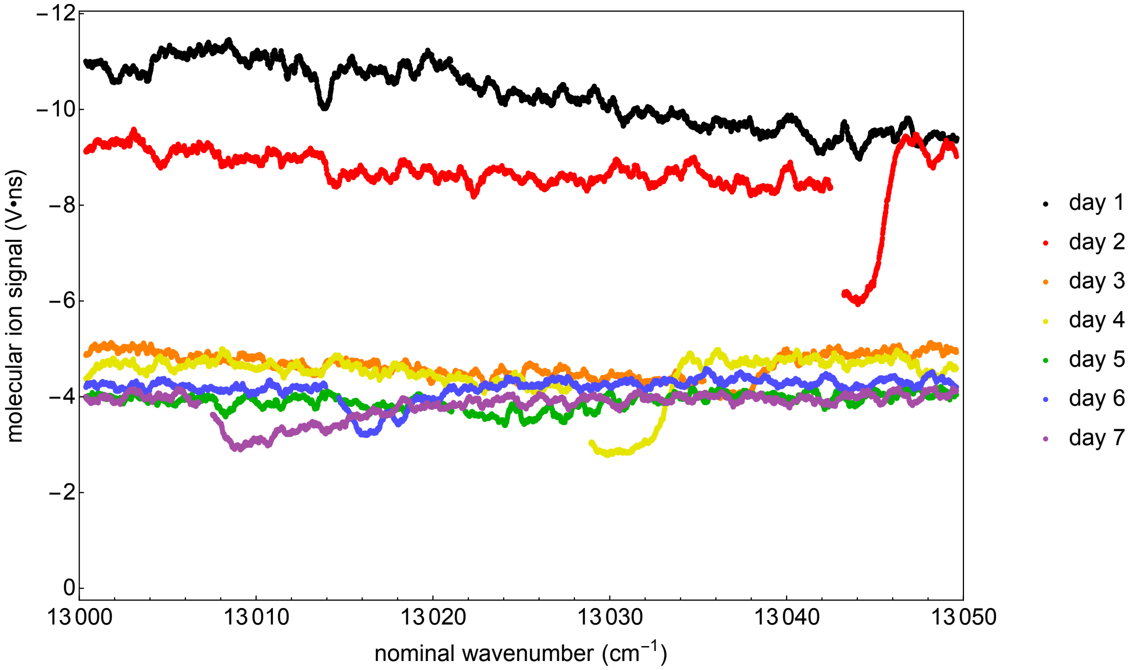

Figure 3.2: Plot of the molecular ion signal for each day of data. To decrease noise, a running average of 50 data points is plotted in each series. Typical spread was 2 V·ns.

power surge in the REMPI beam was later disproven. We diagnosed the cause of the ramp-up time of molecular ions to be a slightly leaky connection in the oxygen line from the canister to the vacuum chamber which causes the tube to lose pressure as it sits in between use. By adding a simple valve in the oxygen line and purging the line before starting a scan, we eliminated this issue.

After concluding the long scan, we played around with different ways to increase the molecular ion production, which was so low that the ion fraction was a good metric; we had dropped to only 15% of shots producing any ions at all. The REMPI beam was well-aligned through the chamber, but we noticed the focusing lens had a line of damage through its center. Adjusting the translation of the lens, we increased to 45% and -5 V·ns. This was better, but still far off from what we knew we could reach. We figured that running scans for days on end had perhaps deformed the shape of the teflon poppet in the gas valve, so we broke vacuum to replace it, then

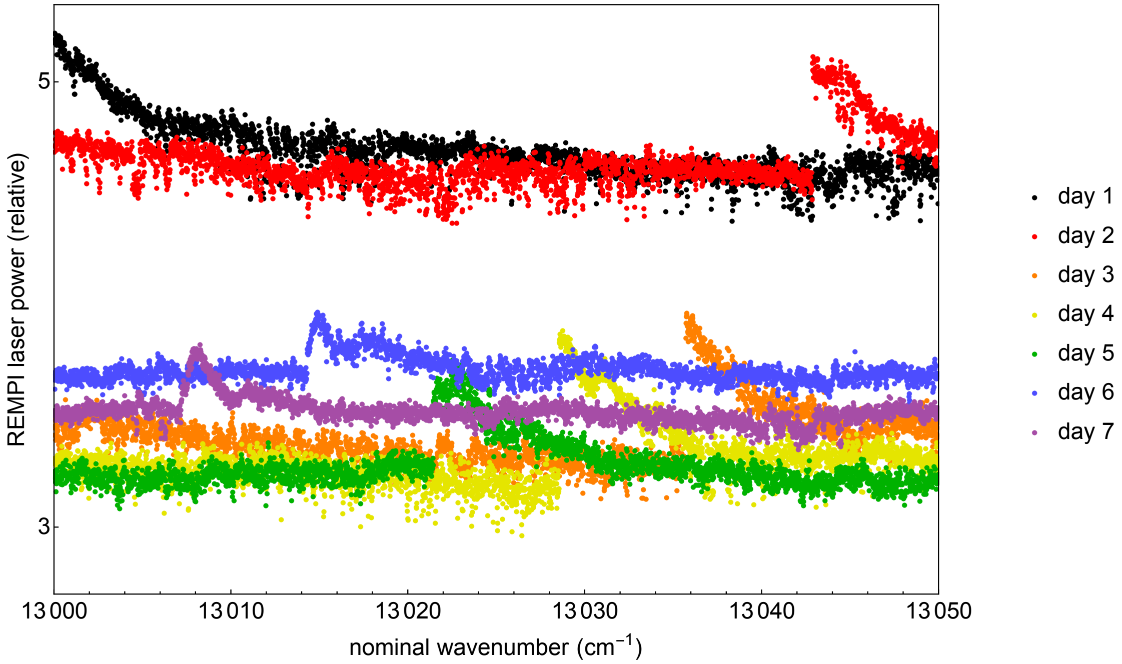

Figure 3.3: Plot of the REMPI laser power each day.

spun the turbo pumps back up overnight. The following day we were at 50% ions and -6 V·ns—unfortunately not much of a change. We tried adjusting the timing and duration of the gas trigger, since replacing the poppet could have affected the shape and timing of the gas pulse. We settled on keeping the timing delay at 600 µs and shifting the duration from 130 µs to 125 µs. Next we adjusted the focus of the ion beam in the TOFMS by changing the Einzel lens voltage from 1600 V to 1450 V. Lastly, we increased the REMPI power by adjusting the focus of the 602 nm light into the frequency doubling crystal (no change) and translating the beam vertically for a gain from 80% ion production and -12 V·ns to 100% ion production and -46 V·ns. In total, this ion integral is a factor of 4 better than we started the scan at and a factor of 11 better than we ended the scan!

Transition laser power

From days 1 and 2 of the scan it was clear that the transition laser power was getting way too low, as seen in Fig. 3.4. We typically run around 40 mJ out of the dye laser, which corresponds to about 20 mJ into the vacuum chamber. At the end of the first day the energy had dropped to 30 mJ. The mechanism for dye lasers losing energy over time is that the dye molecules get broken up and stop contributing to the gain medium. Different dyes have different lifetimes; the Rhodamine dye in the REMPI laser only needs to be changed once every few years, while the Styryl 8 dye in the transition laser has a much shorter lifetime and depletes appreciably over the course of hours. Because it takes about two hours to completely exchange the dye in the Sirah Cobra Stretch, we keep a dye concentrate on hand which we use to top up the active dye on a regular basis by adding a few mL at a time. However, when we added 13 mL of dye to the main amplifier dye circuit, we quickly saturated and were only able to reach 31.7 mJ. We ran with this for one more day, but by the end of day 2 we were down to a mere 14.3 mJ. Adding 10 mL of dye, we decreased to 10.0 mJ. We actually ran a day of data at this level and caused the energy to drop to 2 mJ, but did not include that day in our analysis.

We were clearly over-saturated in the main amplifier dye circuit, but were still dropping in power every day. One explanation was that we actually needed to add dye to the pre-amp dye circuit. As seen in Fig. 3.5, the oscillator and pre-amp use a separate dye cell from the main amplifier, and the two cells have different dye circuits with different concentrations. In general, the pre-amp/oscillator circuit should have a higher concentration than the main amp circuit (150 mg/l in the pre-amp/oscillator and 18.75 mg/l in the main amplifier). It also depletes at a much slower rate because most of the pump light is directed into the main amplifier. However, it seemed it was finally time to top up the pre-amp/oscillator circuit, which had not been touched since installation almost 2.5 years prior.

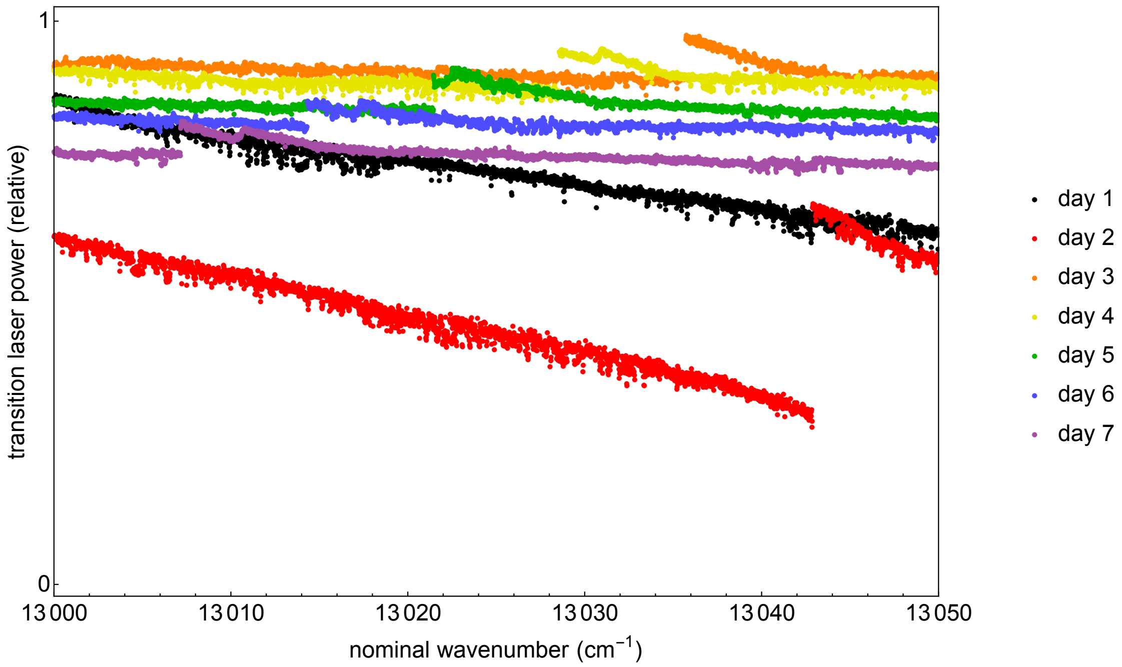

Figure 3.4: Plot of the transition laser power each day. The end value on day 2 (6/7 the way through) was 14.3 ± .2 mJ, and the highest value on day 3 (5/7 of the way through) was at 44.8 ± .7 mJ.

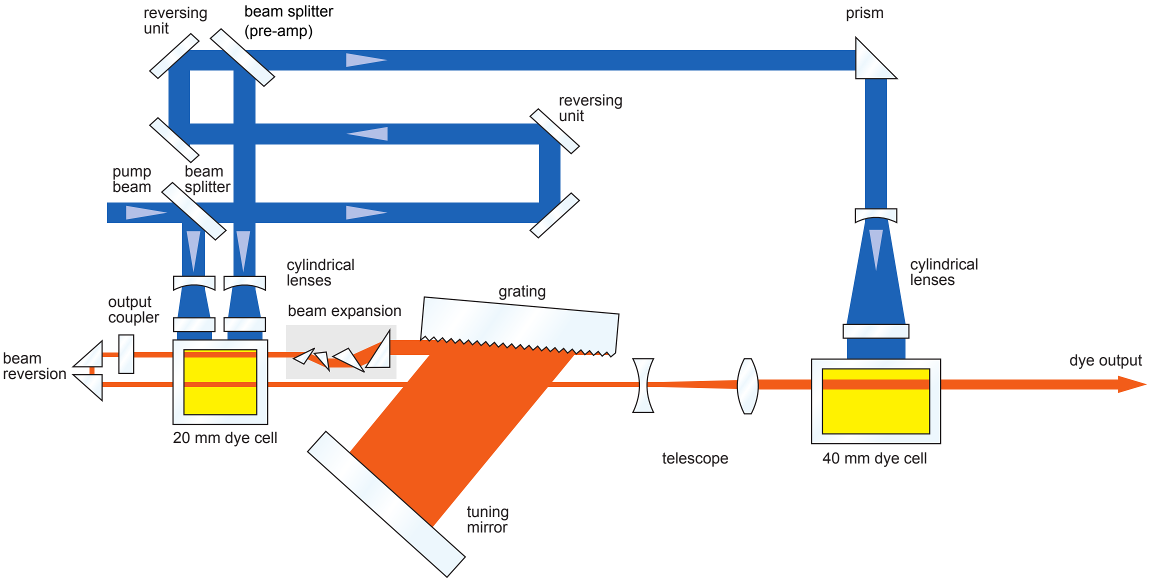

Figure 3.5: Optical layout of the transition laser (Sirah Cobra Stretch). The 20 mm dye cell is the pre-amp and oscillator and the "40 mm" dye cell is the main amplifier, which for us is a 5 mm diameter capillary cell. Figure from [32].

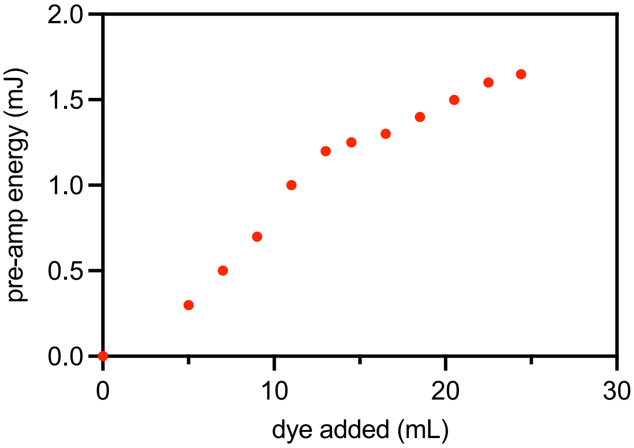

Figure 3.6: Topping up the pre-amp dye of the transition laser. Data taken with the main pump light blocked, but the main amp still installed in the laser. Before adding any dye, the pre-amp was not lasing and the full laser was producing 2 mJ. After adding 24.5 mL to the pre-amp, the total output was 44.8 ± .7 mJ.

To top up the pre-amp/oscillator dye circuit, we closed an internal shutter in the laser to block the pump light to the main amplifier and put a power meter just outside the laser box. The laser initially did not lase, but began lasing immediately after adding dye concentrate and continued to increase in energy as shown in Fig. 3.6. We stopped adding concentrate after reaching a pre-amp and oscillator energy of 1.65 ± .54 mJ. Re-opening the shutter to the main amp, the full lasing energy was 44.8 ± .7 mJ.

We continued onto days 4–7 without adding any more dye to either circuit. As seen in Fig. 3.4, the energy slowly dropped throughout the course of the remaining scans, but remained at a workable level.

3.2.2 Transition data

The data from the narrow O^+ bin in the long scan are shown in Fig. 3.7 next to the simulated spectrum. To process the data, the ion integral at each wavenumber was averaged over the seven days of data. As explained previously, the bandwidth of the laser and the step size of the scan meant any features in the data would be 5 points wide. This does not happen in the data set, so we can conclude that either there is an error in the experiment which makes it incapable of driving the transition, or the transition signal is below the noise in our data from background gas.

Another test of the physicality of the data is to compare it to an artificial data set, as seen in Fig. 3.7. This scrambled signal was created by randomizing each day's data in wavenumber and then averaging over the seven days. In Fig. 3.7 the two sets of data look very similar.

3.3 Signal to noise statistics

Up to this point we have not been able to observe the transition spectrum of our target two-photon transition. We would like to put a limit on what this means for the transition rate. Given a probability of a background signal P_b, the standard deviation of the background σ, and the number of shots N, we can put a limit on the probability of the signal P_s. Noting that the total number of signal points is P_sN, we assert this must be less than σ or we would have been able to see the signal. Thus

$$\begin{aligned}
P_sN &< \sigma = \sqrt{(P_s+P_b)N} && (3.1)\\
\sqrt{N} &< \frac{\sqrt{P_s+P_b}}{P_s} && (3.2)\\
N &< \frac{P_s+P_b}{P_s^2} && (3.3)\\
NP_s^2 - P_s - P_b &< 0 && (3.4)\\
P_s &< \frac{1+\sqrt{1+4NP_b}}{2N}, && (3.5)
\end{aligned}$$

where in the last line we have chosen the positive root as the maximum value for P_s.

If we assume (incorrectly) that our experiment functioned as designed, we can run this calculation. In our case, $P_b = 0.03$ and the long scan had $N = 602$. Thus we find $P_s < 0.0079$, which is a signal to noise ratio of $S < 26\%$. To reiterate, this is

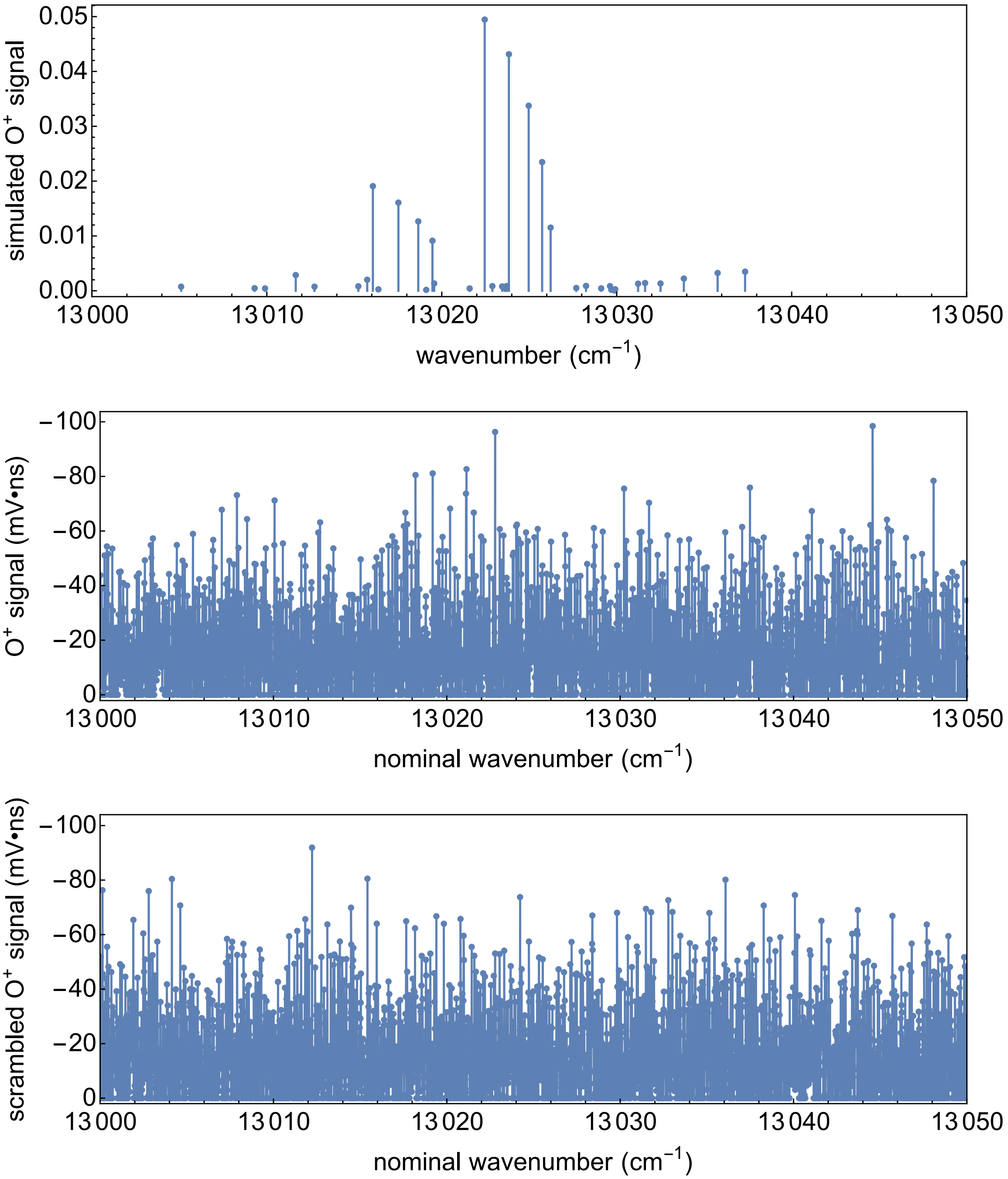

Figure 3.7: Simulated spectrum (top) compared to data from the long scan (middle) and a version of the data artificially scrambled during processing (bottom). The vibrational spectrum is not evident in these data. Additionally, the data are indistinguishable from a random signal.

the limit we *could* set if our experiment were perfect. To find the minimum signal to noise ratio S_x required for an $x\sigma$ result, we can rework the math above and find

$$S_x = \frac{x^2}{2NP_b}\left(1 + \sqrt{1 + \frac{4NP_b}{x^2}}\right). \tag{3.6}$$

With our current background and the same number of data points, this gives $S_2 = .59$, $S_3 = 1.0$, $S_4 = 1.5$, and $S_5 = 2.1$.

3.4 Rabi frequency calculation

A useful metric from our data is a back-calculation of the Rabi frequency for comparison with the theoretical value in Eq. 2.6. The probability of ending up in the excited state $|X^2\Pi_g, v = 16\rangle$ when starting from the ground state $|X^2\Pi_g, v = 0\rangle$ is given by

$$P_s(t) = \sin^2\left(\frac{\Omega_R t}{2}\right), \tag{3.7}$$

where Ω_R is the Rabi frequency of the transition and t is the driving time. Rearranging and substituting our experiment's parameters, we have

$$\begin{aligned}
\frac{\Omega_R}{2\pi I} &= \frac{\arcsin\left(\sqrt{P_s(t)}\right)}{\pi I t} && (3.8)\\
&< \frac{\arcsin\left(\sqrt{.0079}\right)}{\pi(1.8\times 10^{16}\ \mathrm{W/m^2})(7\ \mathrm{ns})} && (3.9)\\
\frac{\Omega_R}{2\pi I} &< 2.2\times 10^{-10}\ \frac{\mathrm{Hz}}{\mathrm{W/m^2}}. && (3.10)
\end{aligned}$$

This places a limit on the transition rate 430 times smaller than the theoretical value calculated in *Atoms* [18],

$$\frac{\Omega_R}{2\pi I} = 9.6\times 10^{-8}\ \frac{\mathrm{Hz}}{\mathrm{W/m^2}}. \tag{3.11}$$

The discrepancy between our experimental value and the *Atoms* value needs to be reconciled. One of the largest sources of potential error in our calculation is the size of the beam waist at its focus. Because the intensity scales inversely with the square of the beam waist (see Eq. 2.3), a beam waist which is a factor of 10 larger than our cited value of 9.8 μm results in

$$\frac{\Omega_R}{2\pi I} < 2.2 \times 10^{-8}\ \frac{\text{Hz}}{\text{W/m}^2}. \tag{3.12}$$

This is the same order of magnitude as the *Atoms* value, but suggests that either the *Atoms* value is larger than the true value or there are other aspects of our experiment (e.g. the dissociation cross section) which are limiting the transition rate more than we have modeled. If we can better constrain our experimental parameters, a second long scan would put a physical limit on this transition rate.

Chapter 4

Conclusion

4.1 Summary of improvements

We have made significant improvements in the apparatus over the past year, including many since the long scan of the vibrational spectrum.

Theory

We updated the PGOPHER simulations from Boran Kuzhan [24] by making a few changes in the constants selected from the literature. Most notably, we included the additional possibility for $J = \frac{9}{2}$ in the ground state $|X^2\Pi_g, v = 0\rangle$ upon re-examination of the state preparation from the neutral molecule. These new states give more transition lines in the spectrum (77 instead of 56).

We began to analyze how the discrete form of the ions is encoded in the voltage integral data we record and now have a better understanding of the distribution of raw signals. This will help us determine a more accurate description of the statistical significance of our results.

We made noteworthy further investigation into the mystery signal started by Annika Lunstad [28], which is a prominent signal in the 39–44 amu time bin. While we thought that the signal may be helpful for aligning the foci of the laser beams, we ruled out this possibility with further experimentation. For this reason I do not discuss the mystery signal in this thesis, although my inquiries examined the signal's dependencies on the lasers, gas levels, and focus position of the beams in the vacuum chamber. Additionally, I characterized an observed double-peak behavior.

Lasers

We installed a new achromatic lens before the vacuum chamber in place of a homemade one. This improved the focusing and spatial overlap of the three laser beams in the vacuum chamber as well as reduced effects from non-diffraction-limited optics.

We increased the molecular ion production dramatically by stabilizing the pump source to the REMPI dye laser and increasing conversion efficiency for more power in the 301 nm pulse. Additionally, we eliminated the initial rise time of 45 minutes by adding a valve to purge the oxygen line before starting a scan.

We came to a better understanding of the transition laser's optimal dye concentrations in the pre-amp and main amplifier circuits, resulting in better practices for topping up the dye concentrations to maintain high power. We also adjusted the voltage on the pockels cell of the InnoLas Nd:YAG laser for increased output after installing a beamsplitter to pump the REMPI laser with the InnoLas.

Data-taking and analysis

We installed new oscilloscopes and pick-offs to track the relative energy of our three lasers throughout a scan. This improves our ability to troubleshoot issues without interrupting a scan by inserting a power meter in one of the beamlines and gives us the option of incorporating laser energies in our analysis.

We installed a new, more accurate wavemeter and developed code to record the wavenumber of the transition laser in each step of a scan. This is a necessary capability for precise measurement of the two-photon vibrational spectrum. Additionally, the wavemeter and some of this new code will be utilized by the Hunter lab.

Lastly, we conducted our first long scan with a hope to see the vibrational spectrum. While we have yet to achieve this goal, the data collected serve as a useful benchmark for the sensitivity of our apparatus and are key to planning future scans.

4.2 Next steps

The upgrades to our experiment in the past year and analysis of the first long scan data give us a clear path forward to further improvements in sensitivity. Specifically, we want to experiment with overlapping the laser pulses in time and using an alternate wavelength for dissociation.

Overlap pulses

As discussed in §2.4.2, there is some concern about the forward motion of the gas molecules during the pulse chain because the distance traveled is on the order of the size of the laser beams. Currently we stagger the pulse arrival times to avoid systematic effects such as an AC Stark shift affecting the transition spectrum. However, given that we have not yet observed the transition, it is perhaps best to focus on getting some signal now before worrying about side effects.

An alternative to overlapping the pulses in time is to stagger them in space, such that the focus of each pulse follows the trajectory of the molecules. At this point, however, we do not have a reliable way of determining the overlap of the beams, let alone a way to make a precise µm-scale adjustment to their focus. This is perhaps even more reason to overlap the beams in time; it may be that the beams are staggered in space in the exact worst order.

Switch dissociation lasers

A limit we are coming up against in our ability to take data is the signal to noise ratio of our system. A large part of the background O^+ we see comes from the dissociation laser. While we have limited the power of the dissociation laser to minimize the background, we also have the option of switching to a 355 nm laser for dissociation from the currently used 266 nm laser. In the past, the 355 nm laser has demonstrated a significantly reduced amount of background O^+ generation.

In the long term, it may be that the 266 nm light has a preferable dissociation cross section as discussed in §2.5. For this reason it would be useful to investigate the pathway by which 266 nm light generates such a high background concentration of O^+ and possible ways to counteract this effect.

Final thoughts

The work done for this thesis has moved our experiment into the regime of a possible first detection of an electric-dipole forbidden two-photon transition in molecular vibrations. After making the changes outlined above, we will run more long scans in search of the vibrational spectrum. Moving forward, the continued improvements of our apparatus will bring our experimental sensitivity beyond the theoretical calculation of the transition moment. This will lead either to a physical limit on the transition moment or an experimental observation of the transition in the near future.

Appendix A

Second Harmonic Generation in the REMPI Beamline

In the REMPI beamline, we use a nonlinear crystal to produce 301 nm light from 602 nm light via second harmonic generation (SHG). As discussed in §2.3, we switched the SHG crystal from KD*P to BBO. One important functional part of the REMPI beamline is the ability to scan the frequency of the dye laser to scan the REMPI spectrum, which allows us to find and select the rotational and vibrational energy levels we prepare the O_2^+ molecules in at the beginning of our experiment.

A primary factor in realizing SHG is phase-matching the fundamental and second harmonic frequencies in the crystal. Due to dispersion, the two wavelengths do not necessarily have the same indices of refraction, and thus can develop a phase-mismatch as they propagate through the crystal which works against the desired conversion. However, because BBO is birefringent and the incident light is linearly polarized, we can orient the crystal's optical axis in the plane of the table such that the (vertically polarized) incident beam is ordinarily polarized (i.e. has polarization perpendicular to the optical axis). This ensures the fundamental frequency has an index of refraction independent of the crystal angle. The second harmonic is then extraordinarily polarized (i.e. has polarization with a component parallel to the optical axis) and has an index of refraction dependent on the angle of the optical axis (and thus the crystal angle). By mounting the crystal on a rotating stage and rotating it in the plane of the table, we are able to adjust the index of refraction of the second harmonic and phase-match the two beams.[1]

A.1 Compensating crystal length calculation

When scanning the REMPI spectrum, the frequency of the incident light is continually changing, which changes the phase matching of the fundamental and second harmonic beams. Thus we require the ability to continually rotate the SHG crystal throughout the scanning process. For this reason the tuning stage is motorized, but there is an additional consideration: changing the angle of incidence displaces the beam horizontally, misaligning all of the optics downstream of the SHG crystal. The scheme to compensate for this effect is quite neat: we simply have a second crystal, called the compensating crystal, which counter-rotates on a stage interlocked with the SHG crystal's stage. This compensating crystal is made of fused silica (FS, the same material as some vacuum windows) and does not affect the wavelength of the light, but does create a displacement. The net effect of the two crystals is to stabilize the resultant beam path, as demonstrated in Fig. A.1.

The displacement of a beam Δx traveling through a crystal is

$$\Delta x = \ell \sin \left(1 - \frac{\cos\theta}{\sqrt{n^2 - \sin^2\theta}} \right), \tag{A.1}$$

where ℓ is the length of the crystal, n is the index of refraction, and θ is the angle of incidence [33]. In order to minimize the total displacement of the beam after traveling

---

[1] Note that this does not necessarily spatially overlap the beams' intensity profiles; that is complicated by walk-off.

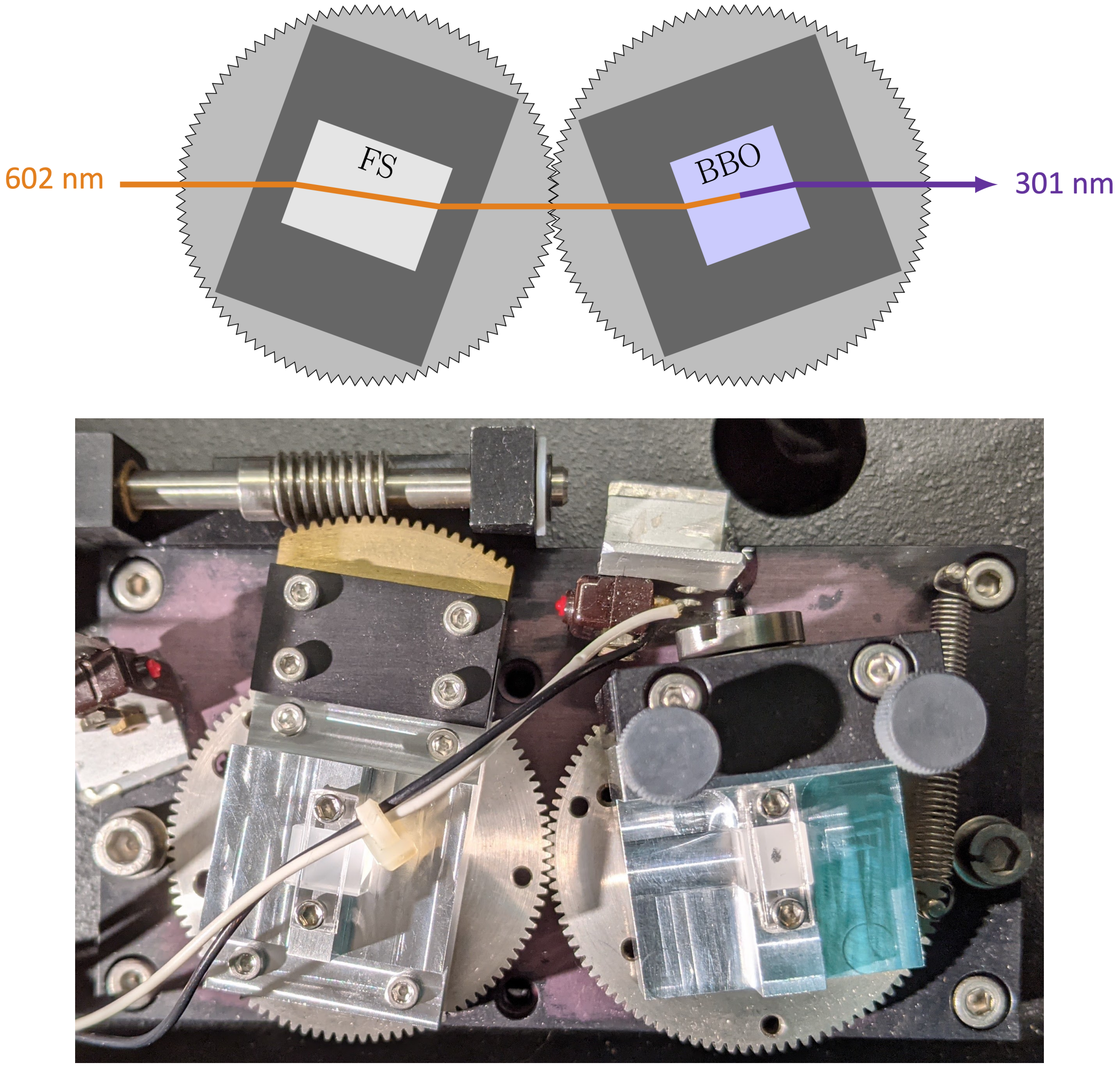

Figure A.1: Counter-rotating scheme of the compensating crystal (fused silica) and the SHG conversion crystal (BBO). Above is a diagram of the beam displacement cancellation and below is a picture of the crystals installed on their rotating stages. Note the dot on the top of the BBO crystal which indicates the direction of polarization of the fundamental frequency.

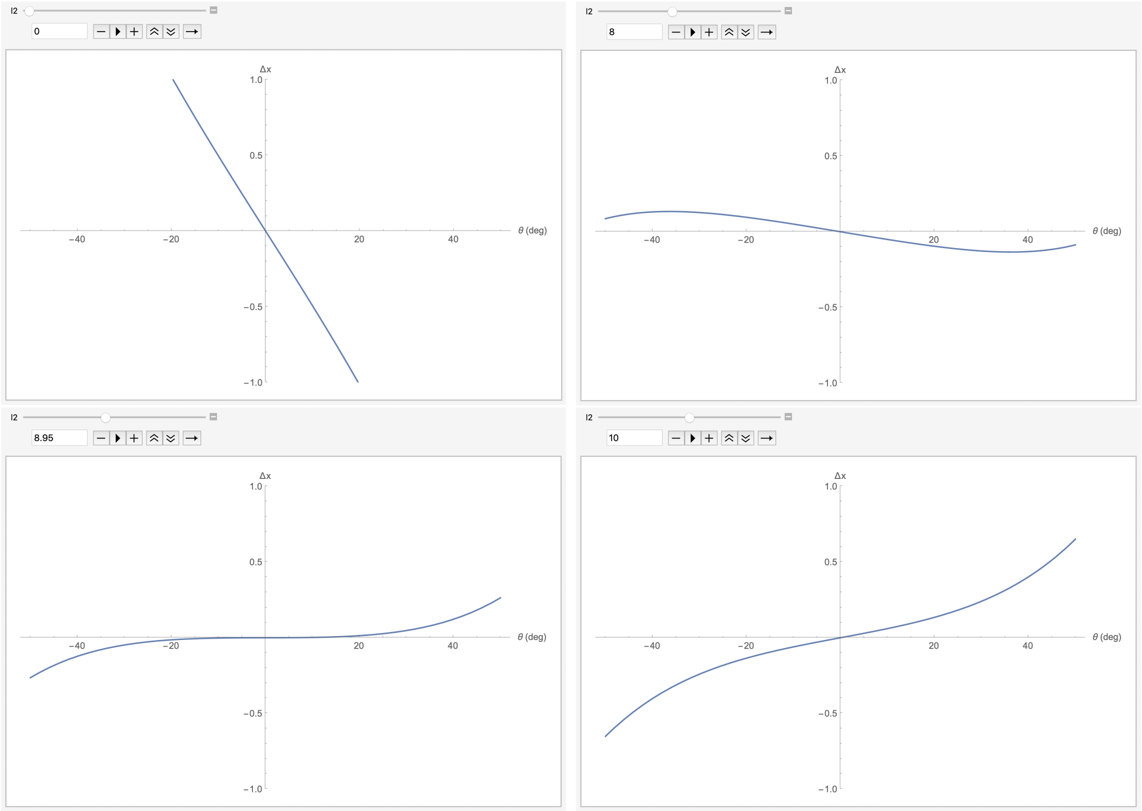

l2 0

l2 8

l2 8.95

l2 10

Figure A.2: Determining the length of the FS compensating crystal for a BBO crystal 7 mm long. From left to right, top to bottom, the length of the crystal is set to 0 mm, 8 mm, 8.95 mm, and 10 mm. The x-axis is the angle of incidence θ in degrees and the y-axis is the lateral beam displacement in mm.

through both the FS and BBO crystals, I wrote a Mathematica notebook to plot the displacement as a function of incidence angle. The length of the crystal is a parameter that can be changed using the sliding control. As evidenced by Fig. A.2, there is no length of crystal which completely eliminates displacement. However, our full scan range for the REMPI spectrum is only between 590 nm and 730 nm, corresponding to phase-matching angles of 41.4° and 32.2° with respect to the optical axis, respectively. By cutting the crystal with the normal incidence at 36.8°, we minimize the required angle tuning to ±4.6°. As seen in Fig. A.2, a 8.95 mm FS crystal effectively eliminates the displacement in this range.

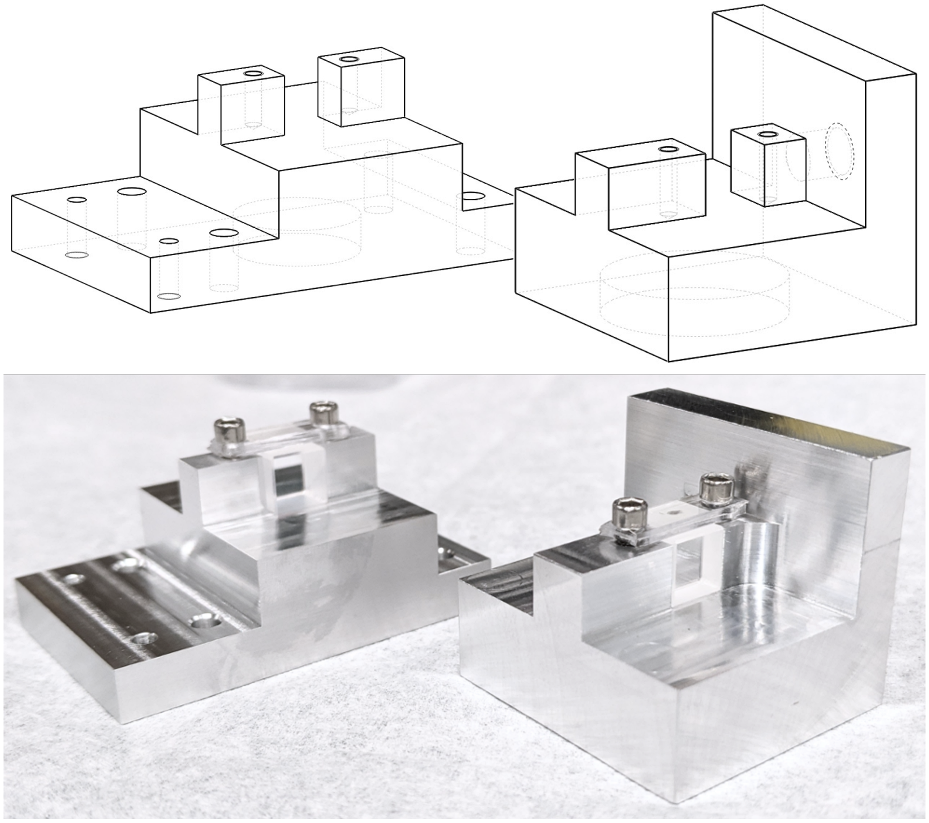

Figure A.3: Crystal mounts for the FS crystal (left) and BBO crystal (right), including the Solidworks designs showing hidden pockets and holes (above) and a photo of the mounts with the crystals installed (below). The mounts are machined out of aluminum and are about 1 in tall each, with a precision of .001 in for the width and height of the channels for the crystals. The crystals are held in place with light pressure from a polycarbonate cap.

A.2 Crystal mounts

Our new crystals required new crystal mounts to attach them firmly to the rotating stages. I took measurements of the old mounts and designed mounts for the new crystal specifications in Solidworks. I then machined the mounts with the help of Amherst's machinist Jim Kubasek. The Solidworks designs and machined products are shown in Fig. A.3.

Appendix B

The Toptica/HighFinesse Wavemeter

It is vital to our experiment to know the frequency of the transition laser throughout the scan. However, the wavemeter we had in the lab was a Burleigh Pulsed Wavemeter from circa 1992 which, understandably, was no longer very reliable. In particular, its wavenumber reading routinely jumped by small (2 cm^{-1}) or large (100 cm^{-1}) amounts and when attempting to calibrate it with a potassium absorption spectrum, we found the most stable reading was 4 cm^{-1} off from true. With this persistent unreliability, it was time for an upgrade.

The new wavemeter is a Toptica/HighFinesse WS7-60 Wavelength Meter with an eight-channel multimode switch. This switch allows us to have optical fibers with our transition laser (pulsed), a calibration laser (continuous), and any other lasers from our lab we wish to measure aligned into the wavemeter at the same time. The wavemeter is also a shared device for the department, and in the long term it will be installed in a separate room with optical fibers from multiple labs routed to it.

In order to integrate the new wavemeter into our experiment, there were two major tasks to accomplish. First, we needed a LabView VI to query the wavemeter

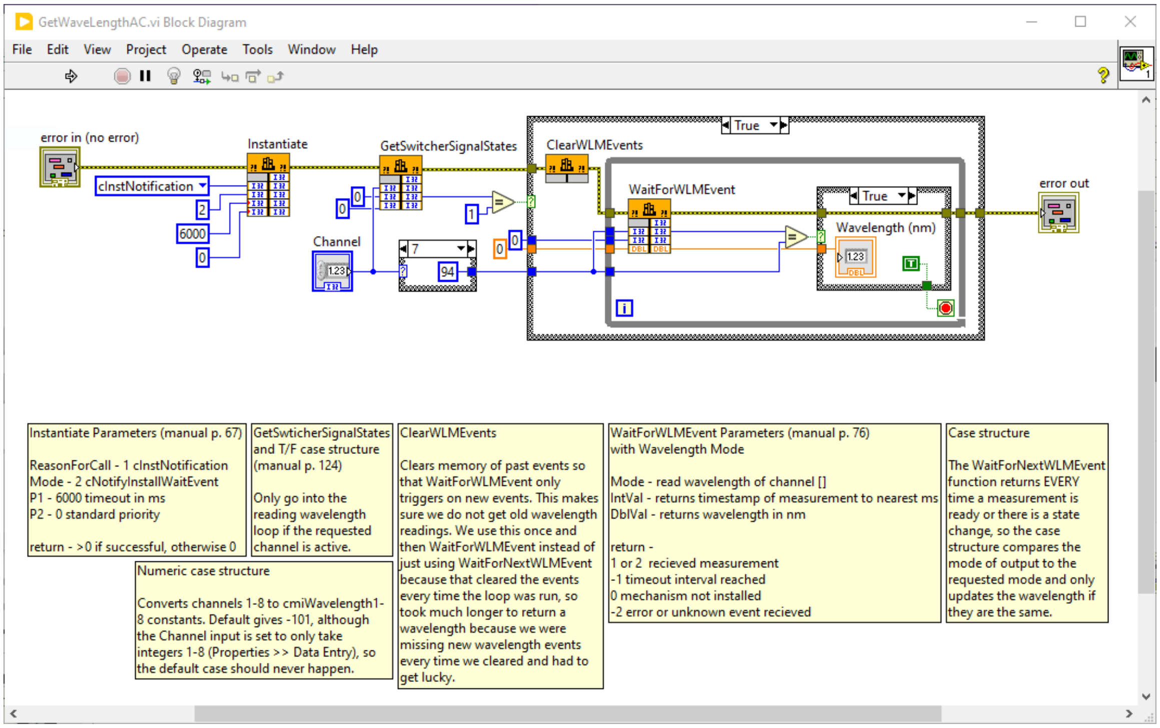

Instantiate Parameters (manual p. 67)

ReasonForCall - 1 cInstNotification
Mode - 2 cNotifyInstallWaitEvent
P1 - 6000 timeout in ms
P2 - 0 standard priority

return - >0 if successful, otherwise 0

GetSwticherSignalStates and T/F case structure (manual p. 124)

Only go into the reading wavelength loop if the requested channel is active.

ClearWLMEvents

Clears memory of past events so that WaitForWLMEvent only triggers on new events. This makes sure we do not get old wavelength readings. We use this once and then WaitForWLMEvent instead of just using WaitForNextWLMEvent because that cleared the events every time the loop was run, so took much longer to return a wavelength because we were missing new wavelength events every time we cleared and had to get lucky.

WaitForWLMEvent Parameters (manual p. 76)
with Wavelength Mode

Mode - read wavelength of channel []
IntVal - returns timestamp of measurement to nearest ms
DblVal - returns wavelength in nm

return -
1 or 2 recieved measurement
-1 timeout interval reached
0 mechanism not installed
-2 error or unknown event recieved

Case structure

The WaitForNextWLMEvent function returns EVERY time a measurement is ready or there is a state change, so the case structure compares the mode of output to the requested mode and only updates the wavelength if they are the same.

Numeric case structure

Converts channels 1-8 to cmiWavelength1-8 constants. Default gives -101, although the Channel input is set to only take integers 1-8 (Properties >> Data Entry), so the default case should never happen.

Figure B.1: LabView VI run on the wavemeter computer which sends a query for the next wavelength reading. Function nodes are used to access the wavemeter's programming.

for the next wavelength reading on a specific channel. Second, we needed another VI to call the first VI over the internet, since the wavemeter, as a shared instrument, runs on a different computer from our main experiment.

B.1 Measuring wavelength

Fig. B.1 is a screenshot of my code for the first of these two tasks. The wavemeter's software has a plethora of useful functions built in, but no stock LabView functionality. Instead, all of the relevant functions are located in a .dll file (dynamic link library). After figuring out the relevant functions, I constructed "call library function nodes" to utilize the functions in LabView. Table B.1 gives detailed instructions for how to do this.

The main aspect of this VI is that it does not report the currently available

Instructions for making a function node.

1. Go to the block diagram of a VI.
2. Right click for the menu, select Connectivity >> Libraries & Executables >> Call Library Function Node.
3. Place the function node on the block diagram, then double-click on it to bring up its dialog box.
4. In the Function tab, set the following:
    - Library name or path: wlmData.dll
    - Function name: select from drop-down menu the name of the function as found in the manual (e.g. WaitForWLMEvent)
    - Thread: Run in UI thread
    - Calling convention: stdcall (WINAPI)
5. Click over to the Parameters tab to edit the function prototype. Also find your function's description in the manual (this tells you the parameter names), as well as its location in the table on p. 146 (this tells you the parameter types). Use the + button to add parameters and the boxes on the right side of the window to edit each Name and Type. Note that after selecting a Type, you may get more options. For example:
    - The description of the WaitForWLMEvent gives the function prototype (in C) long WaitForWLMEvent(lref Mode, lref IntVal, dref DblVal). However, LabView uses slightly different data types. If you don't know what the correct conversion is, reference the table on p. 146.
    - In the table, the type of Arg1 is listed as Int32 (ref). This means that in LabView, the Mode parameter should be set to Type: Signed 32 bit integer with Pass: Pointer to value. If there is no (ref) after the type, just select Pass: Value.
6. Your function node is complete! You will notice that any parameters that seem to just function as outputs (e.g. WaitForWLMEvent's IntVal and DblVal) still need to have something wired to their input on the function node in the block diagram to have a working VI. In this case, create a dummy constant.

Table B.1: Instructions for making a function node. All page numbers refer to [34].

Code	Name	Description
0	ErrNoValue	the requested channel is not active
-1	ErrNoSignal	there is no signal in the requested channel
-2	ErrBadSignal	the shape of the signal is not recognizable
-3	ErrLowSignal	the signal is undersaturated
-4	ErrBigSignal	the signal is oversaturated

Table B.2: Common errors from the wavemeter. For errors -5 to -29, see [34] p. 157.

wavelength reading, but rather takes the request and returns the next new reading. This is an important distinction because during a scan of the two-photon spectrum, we record the wavelength of the laser at each step. However, the multimode switch on the wavemeter works by continuously cycling between the activated channels. Thus it is possible that the most recently available measurement for a particular channel at the time of request is a measurement corresponding to the previous step. For this reason it is vital to wait for a new measurement.

Sometimes the calibration of the exposure is incorrect, and an error is unavoidable. In this case, the VI is designed to pass out certain error codes, including those given in Table B.2.

B.2 Remote communication with the wavemeter computer

A second LabView VI, shown in Fig. B.2, is required to use the first VI. This is done using the LabView VI server, which allows you to call LabView code on a target computer (here, the wavemeter computer) across the internet and treat it like a subVI in your local code (here, on the main experiment computer). Essentially, by identifying the IP address of the target computer, knowing the file path for the target code, and pre-approving the local computer for access on the target computer, you

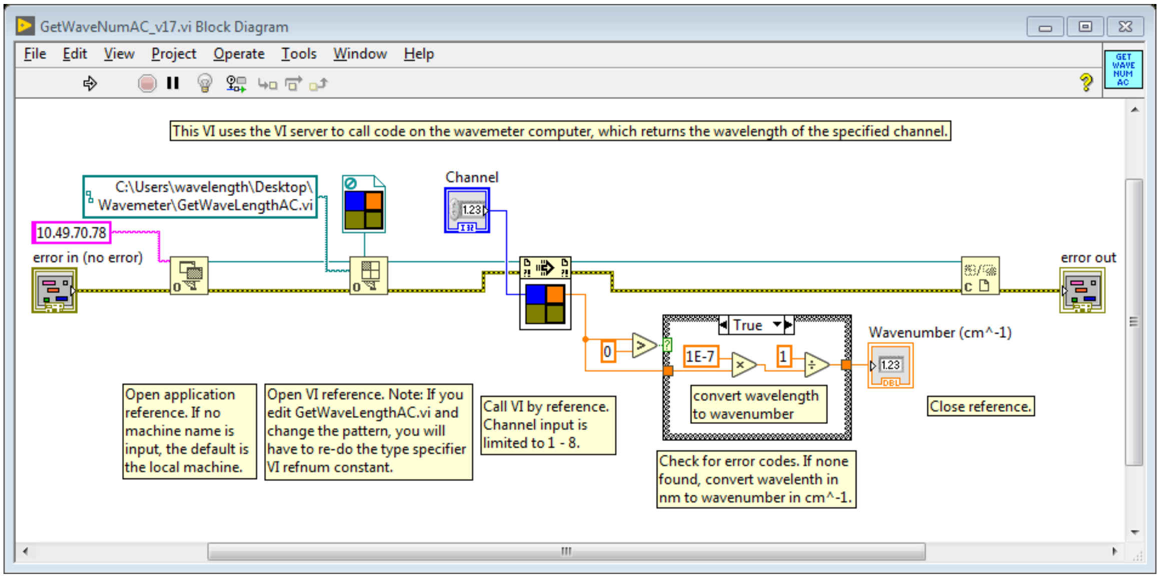

This VI uses the VI server to call code on the wavemeter computer, which returns the wavelength of the specified channel.

Open application reference. If no machine name is input, the default is the local machine.

Open VI reference. Note: If you edit GetWaveLengthAC.vi and change the pattern, you will have to re-do the type specifier VI refnum constant.

Call VI by reference. Channel input is limited to 1 - 8.

convert wavelength to wavenumber

Check for error codes. If none found, convert wavelenth in nm to wavenumber in cm^-1.

Close reference.

Figure B.2: LabView VI which runs on the main experiment computer and calls GetWaveLengthAC.vi on the wavemeter computer. All of the VI server functions are located on the block diagram function palette under Programming >> Application Control.

can open up a channel of communication between the two computers. The steps for doing so are described in Table B.3.

This VI is integrated into our main experiment code and is called every time the laser steps wavenumber. It usually takes under 4 seconds to run, which is enough to run a second time if it receives an error code from the first VI. If the error persists, it is passed out for handling later as useful information about the wavemeter calibration. If it receives a wavelength, it converts the value to a wavenumber, which is our preferred unit.

Note that the run time is determined not by the LabView code, but by our long exposure time. The channel switch has a very low damage threshold, so we have to attenuate our pulsed lasers significantly and then integrate over multiple pulses, which occur at a rate of 10 Hz. Run time should not be an issue for use with continuous-wave lasers.

	Instructions for enabling remote access.
1.	Find the IP address of your local computer. If there is more than one IP address (say, for a private internet service), you may need that IP address as well.
2.	Open LabView on the target computer. In the menu bar, select Tools >> Options... >> VI Server.
3.	Under Protocols, check the box for TCP/IP.
4.	Under Machine Access, add the IP address of the local computer. You should only need one, but you may need a different one than you think. If you get an error saying that the local computer failed a security check, add a different IP address.

Table B.3: Instructions for enabling remote access. This is a prerequisite for using the LabView server. In our experiment, the local computer refers to the computer on which the experiment code is run, and the target computer refers to the wavemeter computer, which houses the code for taking wavelength measurements.

Bibliography

[1] M. Baak, , M. Goebel, J. Haller, A. Hoecker, D. Kennedy, R. Kogler, K. Mönig, M. Schott, and J. Stelzer, "The electroweak fit of the standard model after the discovery of a new boson at the LHC," The European Physical Journal C **72** (2012), URL `https://doi.org/10.1140%2Fepjc%2Fs10052-012-2205-9`.

[2] G. Gabrielse, "The standard model's greatest triumph," Physics Today **66**, 64 (2013), `https://doi.org/10.1063/PT.3.2223`, URL `https://doi.org/10.1063/PT.3.2223`.

[3] R. Escribano and E. Massó, "High precision tests of QED and physics beyond the standard model," The European Physical Journal C **4**, 139 (1998), URL `https://doi.org/10.1007%2Fpl00021656`.

[4] ACME Collaboration, V. Andreev, D. G. Ang, D. DeMille, J. M. Doyle, G. Gabrielse, J. Haefner, N. R. Hutzler, Z. Lasner, C. Meisenhelder, B. R. O'Leary, C. D. Panda, *et al.*, "Improved limit on the electric dipole moment of the electron," Nature **562**, 355 (2018).

[5] T. S. Roussy, D. A. Palken, W. B. Cairncross, B. M. Brubaker, D. N. Gresh, M. Grau, K. C. Cossel, K. B. Ng, Y. Shagam, Y. Zhou, V. V. Flambaum, K. W. Lehnert, *et al.*, "Experimental Constraint on Axionlike Particles over Seven Orders of Magnitude in Mass," Physical Review Letters **126**, 171301 (2021), URL `https://link.aps.org/doi/10.1103/PhysRevLett.126.171301`.

[6] G. Gabrielse, D. Hanneke, T. Kinoshita, M. Nio, and B. Odom, “New Determination of the Fine Structure Constant from the Electron g Value and QED,” Physical Review Letters **97**, 030802 (2006), ibid. **99**, 039902(E) (2007).

[7] E. Cornell, “The Three-Legged Stool,” in “Proceedings of the 2020 APS April Meeting,” (2020), URL `https://meetings.aps.org/Meeting/APR20/Session/A01.3`.

[8] D. DeMille, J. M. Doyle, and A. O. Sushkov, “Probing the frontiers of particle physics with tabletop-scale experiments,” Science **357**, 990 (2017), ISSN 0036-8075.

[9] J. Liu, X. Chen, and X. Ji, “Current status of direct dark matter detection experiments,” Nature Physics **13**, 212 (2017), URL `https://doi.org/10.1038%2Fnphys4039`.

[10] S. Kotochigova, T. Zelevinsky, and J. Ye, “Prospects for application of ultracold Sr_2 molecules in precision measurements,” Physical Review A **79**, 012504 (2009).

[11] E. J. Salumbides, J. C. J. Koelemeij, J. Komasa, K. Pachucki, K. S. E. Eikema, and W. Ubachs, “Bounds on fifth forces from precision measurements on molecules,” Physical Review D **87**, 112008 (2013).

[12] R. H. Parker, C. Yu, W. Zhong, B. Estey, and H. Müller, “Measurement of the fine-structure constant as a test of the Standard Model,” Science **360**, 191 (2018).

[13] T. Bothwell, C. J. Kennedy, A. Aeppli, D. Kedar, J. M. Robinson, E. Oelker, A. Staron, and J. Ye, “Resolving the gravitational redshift across a millimetre-scale atomic sample,” Nature **602**, 420 (2022), URL `https://doi.org/10.1038%2Fs41586-021-04349-7`.

[14] A. D. Ludlow, M. M. Boyd, J. Ye, E. Peik, and P. O. Schmidt, "Optical atomic clocks," Reviews of Modern Physics **87**, 637 (2015).

[15] F. Riehle, P. Gill, F. Arias, and L. Robertsson, "The CIPM list of recommended frequency standard values: guidelines and procedures," Metrologia **55**, 188 (2018).

[16] D. Hanneke, B. Kuzhan, and A. Lunstad, "Optical clocks based on molecular vibrations as probes of variation of the proton-to-electron mass ratio," Quantum Science and Technology **6**, 014005 (2021), `2007.15750`.

[17] T. E. Wall, "Preparation of cold molecules for high-precision measurements," Journal of Physics B **49**, 243001 (2016).

[18] R. Carollo, A. Frenett, and D. Hanneke, "Two-Photon Vibrational Transitions in $^{16}O_2^+$ as Probes of Variation of the Proton-to-Electron Mass Ratio," Atoms **7**, 1 (2018).

[19] M. Safronova, D. Budker, D. DeMille, D. F. J. Kimball, A. Derevianko, and C. W. Clark, "Search for new physics with atoms and molecules," Reviews of Modern Physics **90** (2018), URL `https://doi.org/10.1103%2Frevmodphys.90.025008`.

[20] Y. Stadnik and V. Flambaum, "Can Dark Matter Induce Cosmological Evolution of the Fundamental Constants of Nature?" Physical Review Letters **115** (2015), URL `https://doi.org/10.1103%2Fphysrevlett.115.201301`.

[21] C. M. Western, "PGOPHER: A program for simulating rotational, vibrational and electronic spectra," Journal of Quantitative Spectroscopy and Radiative Transfer **186**, 221 (2017), ISSN 0022-4073, satellite Remote Sensing and Spectroscopy: Joint ACE-Odin Meeting, October 2015, URL `https://doi.org/10.1016/j.jqsrt.2016.04.010`.

[22] J. M. Brown and A. Carrington, *Rotational Spectroscopy of Diatomic Molecules* (Cambridge Univ. Press, 2003).

[23] W. Demtröder, *Atoms, Molecules and Photons: An Introduction to Atomic-Molecular- and Quantum Physics* (Springer Berlin Heidelberg, 2006), ISBN 978-3-540-32346-4, URL `https://books.google.com/books?id=XFyMMtjZzZsC`.

[24] B. Kuzhan, *A Molecular Beam Apparatus to Search for Time-Variation of Fundamental Constants*, Undergraduate thesis, Amherst College (2021).

[25] C. M. Western, "PGOPHER, A Program for Simulating Rotational, Vibrational and Electronic Spectra," URL `http://pgopher.chm.bris.ac.uk`.

[26] W. Kong and J. W. Hepburn, "Rotationally resolved threshold photoelectron spectroscopy of O_2 using coherent XUV: formation of vibrationally excited ions in the Franck–Condon gap," Canadian Journal of Physics **72**, 1284 (1994).

[27] Y. Song, M. Evans, C. Y. Ng, C.-W. Hsu, and G. K. Jarvis, "Rotationally resolved pulsed field ionization photoelectron bands of $O_2^+(X\,^2\Pi_{1/2,3/2g}, v^+ = 0 - 38)$ in the energy range of $12.05 - 18.15$ eV," Journal of Chemical Physics **111**, 1905 (1999).

[28] A. Lunstad, *Driving Forbidden Vibrational Transitions in Molecular Oxygen*, Undergraduate thesis, Amherst College (2021).

[29] J. Pfatteicher, *Developing Rapid Quenching Electronics for Coupling an Ion Trap to a Mass Spectrometer*, Undergraduate thesis, Amherst College (2019).

[30] R. T. Sutter, T. J. Fellers, and M. W. Davidson, "Laser Cavity Resonance Modes and Gain Bandwidth," (2016), URL `https://micro.magnet.fsu.edu/primer/java/lasers/gainbandwidth/index.html`.

[31] P. Jauernik, "Precisionscan and CobraStretch: Data sheet update," (2013).

[32] Sirah Lasertechnik, “Pulsed Dye Laser’s Manual Version 2.0.4,” (2019).

[33] Edmund Optics, “Beam Displacement Calculator,” (2021), URL `https://www.edmundoptics.com/knowledge-center/tech-tools/beam-displacement-calculator/`.

[34] HighFinessse Laser and Electronic Systems, “Wavelength Meter Angstrom WS/7 User Manual,” (2021).